POLITECNICO DI MILANO

School of Industrial and Information Engineering

Master of Science Courses in Biomedical Engineering

COMPUTATIONAL FATIGUE ANALYSIS OF TITANIUM SPINAL RODS

Supervisor: Prof. Tomaso VILLA

Co-supervisor: Ing. Francesca BERTI

Graduation thesis of:

Hugo AGOSTINI Matr. 897431

Academic year 2018-2019

Acknowledgements

I would like to thank my supervisor Tomaso Villa, who allowed me to perform this study.

I would like to thank my co-supervisor Francesca Berti, who helped me at each step of the thesis, with her wise advises and her kindness.

Thanks to my parents and my brother Bastien for their supports during all my studies.

I would like to thank my girlfriend Audrey for her encouragements and her support during all those years, despite difficulties. Thanks also to her parents Chantal and Gilles for their cheerings.

I would like to thank all my friends, Aldo, Yunus, Sarah, Marta, Diana and both Andrea from Politecnico and particularly Antoine, Erwan, Frédéric, Quentin, Kévin, Valentin and Laura from Centrale Lille.

Table of contents

Abstract

Posterior fixation based on spinal rods is the gold standard for the treatment of spinal deformaties. Titanium rods have adequate biocompatibility and mechanical properties, but have a low fatigue strength. The purpose of this study is to develop a validated numerical model of a specific brand of titanium rods, which would be capable of predicting their fatigue behaviour. Six different fatigue configurations (load levels) were simulated mimicking some previous experiments performed in four-points bending configuration. The equivalent Sines stress has been chosen as fatigue index and it was possible to interpret the fatigue output in each configuration. It can be concluded that the numerical analysis herein performed is consistent with the experimental data.

State of Art

In this chapter, the anatomy of the human vertebral column and its diseases will be described. Then, solutions to treat it will be presented.

The human vertebral column

Anatomy

The human vertebral column (also called spine) surrounds the spinal cord and sustains entire body during the movement as well as the static posture. The spine exhibits four curvatures from a lateral view (Figure 1): two of them, the cervical and the lumbar curvatures, are referred as convex while the thoracic and the sacral curvatures are concave.

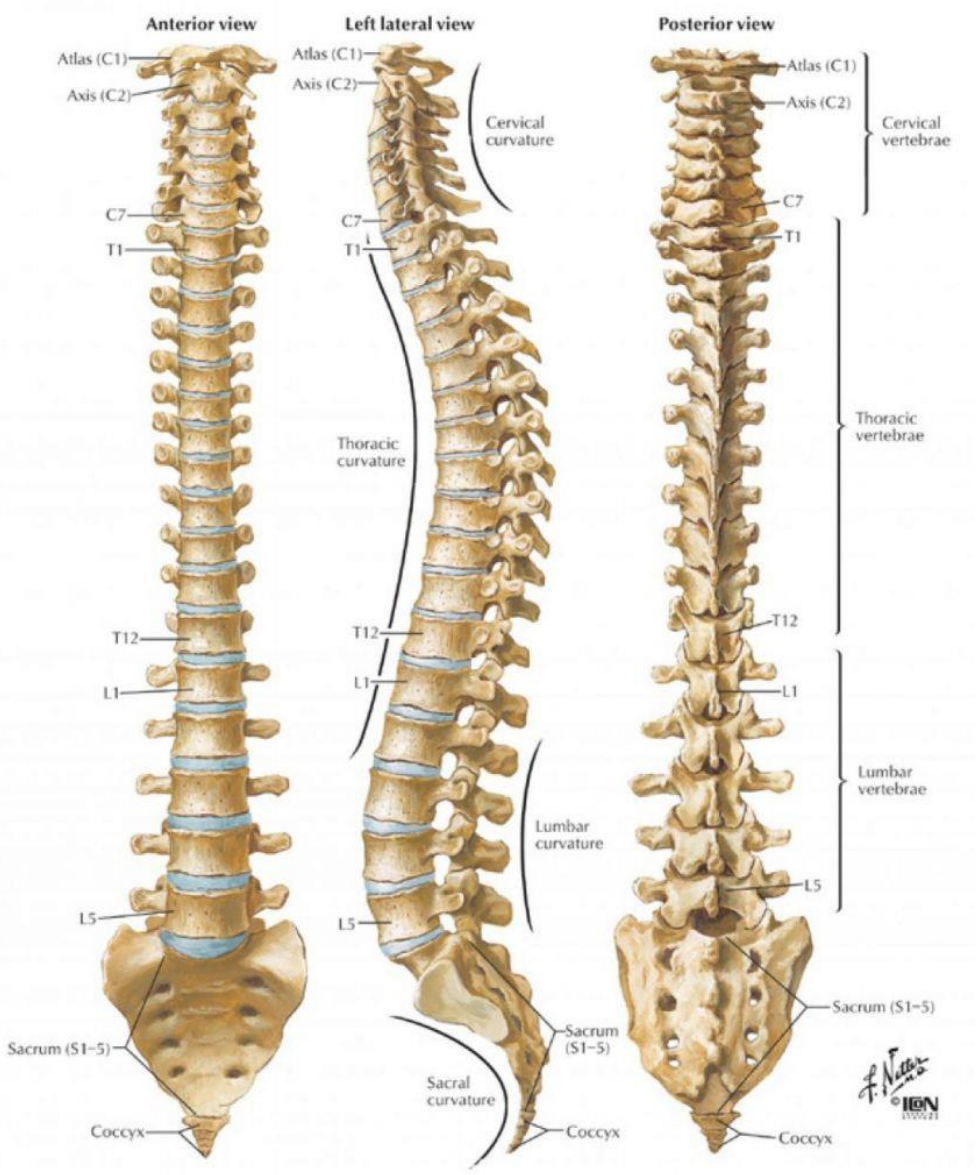

Figure 1: The anatomy of the human vertebral column

The human vertebral column is divided into 5 segments, defined by the aforementioned curvatures. It is made of thirty-three functional units called vertebrae divided as:

- Cervical (C1–C7) which holds the head;
- Thoracic (T1–T12) which holds the chest;
- Lumbar (L1–L5) which holds the abdomen;
- The sacrum (S1–S5) which is a part of the pelvis skeleton;
- The coccyx (Tailbone) which is a part of the pelvis skeleton too.

Vertebrae can differ in size according to the region and are composed of two parts: the vertebral arch that is posterior and the vertebral body that is anterior. Both enclose the vertebral foramen which contains the spinal cord.

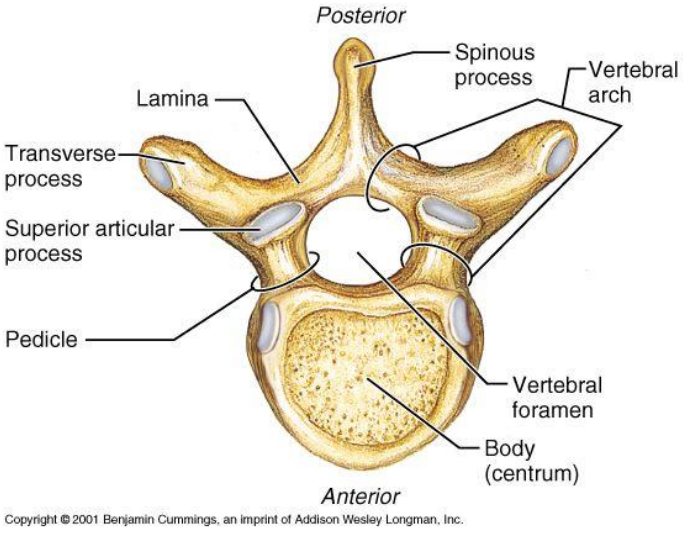

Figure 2: Vertebra structure

The intervertebral disks are placed in between two vertebrae. They consist of an outer fibrous ring, the “anulus fibrosus”, which surrounds an inner gel-like center, the nucleus pulposus [4].Their function is to allow the spine movement by allowing inter-vertebrae displacements . Moreover, they absorb shocks and homogeneously distribute pressures.

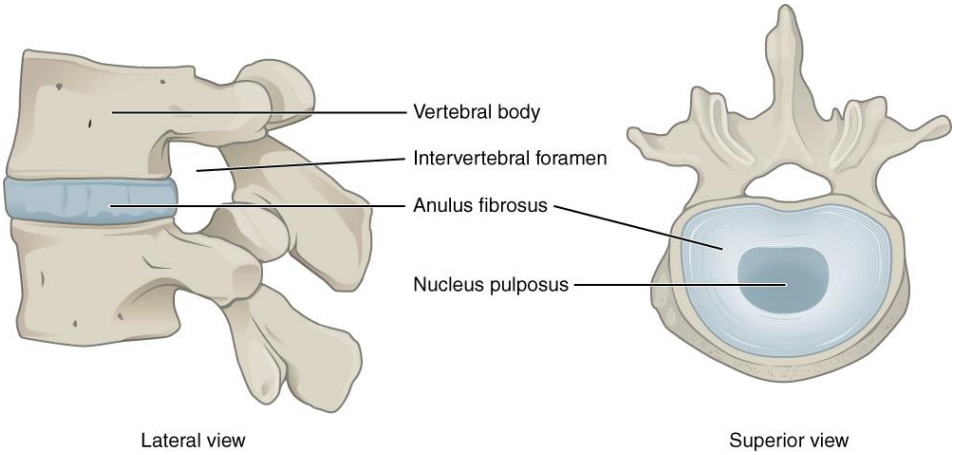

Figure 3: The Anatomy of the intervertebral disc

Diseases

Surgery is the solution of many spinal diseases, since they involve mainly bones deformities and postural impairments. The most common diseases involving surgery can be divided in two categories, those which can be cured thanks to fixation surgery and the others.

Diseases not cured with fixation surgery

- Herniated intervertebral disk

It is an injury to the cushioning and connective tissue between vertebrae, usually caused by excessive strain or trauma to the spine. It may result in back or diffused pain and physical disability [6];

- Vertebral osteochondrosis

Also known as Scheuermann's disease, it is a self-limiting skeletal disorder of childhood in which the vertebrae grow unevenly with respect to the sagittal plane and the posterior angle is often greater than the anterior. This results in the signature "wedging" shape of the vertebrae, causing kyphosis [7];

- Osteoporosis

It is a disease most common among the elderly that reduces the total mass of the bone that becomes porous and fragile. The bone is then more likely to be broken after small shocks [8];

Diseases cured with fixation surgery

- Sagittal plane disorders

They are disorders of the rachis curvature, that can be increased (“curved back”) or decreased (“flat back”). Particularly, an over-curved lumbar region is called lumbar lordosis while an excessive convex curvature of the spine in the thoracic and sacral regions is a thoracic or sacral kyphosis [18]. All these kinds of disorders lead to pain for the patient and back instability;

❖ Degenerative disc disease (discopathy)

It consists of anatomic changes and a loss of function of one or more intervertebral discs of the spine. This may cause symptoms like pain, back rigidity and sensitivity loss in arms and legs. Sugery is involved only when medical treatment and physiotherapy do not relieve chronic pain [5];

❖ Scoliosis

Scoliosis is a medical condition in which the spine has a sideways curve which is usually "S" or "C" shaped over three dimensions. It always involves elemental deformities in the three main planes. In some, the degree of curve is stable, while in others, it increases over time. Mild scoliosis does not typically cause problems, while severe cases can interfere with breathing. It may also prevent organs development during child growth. There is usually no pain, except for severe scoliosis [9].

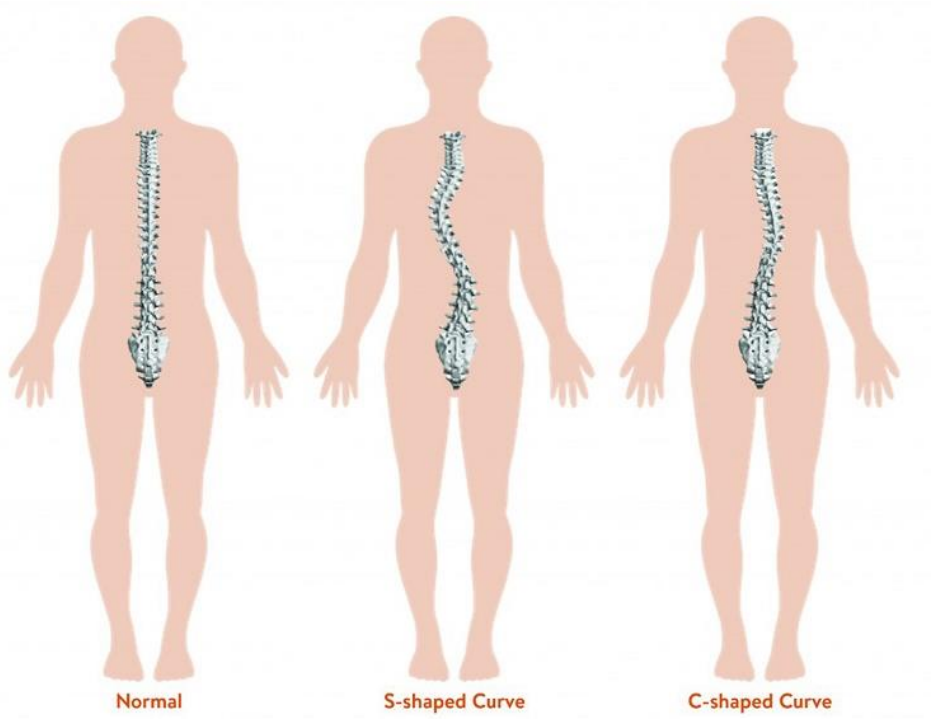

Figure 4: Normal shape of the spine and scoliotic ones

Spinal fixation

Principle and standard rods

Surgery is usually involved to cure all those diseases and improve the quality of life of patients. The most common surgery is the spinal fusion using metallic rods and screws and allowing to link two adjacent vertebrae. There are different kinds of vertebral fusions, depending on the region of the spine involved: anterior lumbar, posterior lumbar and transforaminal lumbar. The type of surgery that should be done is usually figured out thanks to imaging exams, like radiography and tomography.

The standard rods are circular rods in Ti6Al4V, stainless steel or Cr-Co with the properties presented table 1.

Table 1: Mechanical properties of the standard rods' material [10]

Material	Density ($g.cm^{-3}$)	E (GPa)	Yield stress (MPa)	MRI	Notch sensitivity
Stainless Steel	8	190	690	No	Low
Ti6Al4V	4.43	116	795	Yes	High
Cr-Co	7-8	218	800	Yes	-

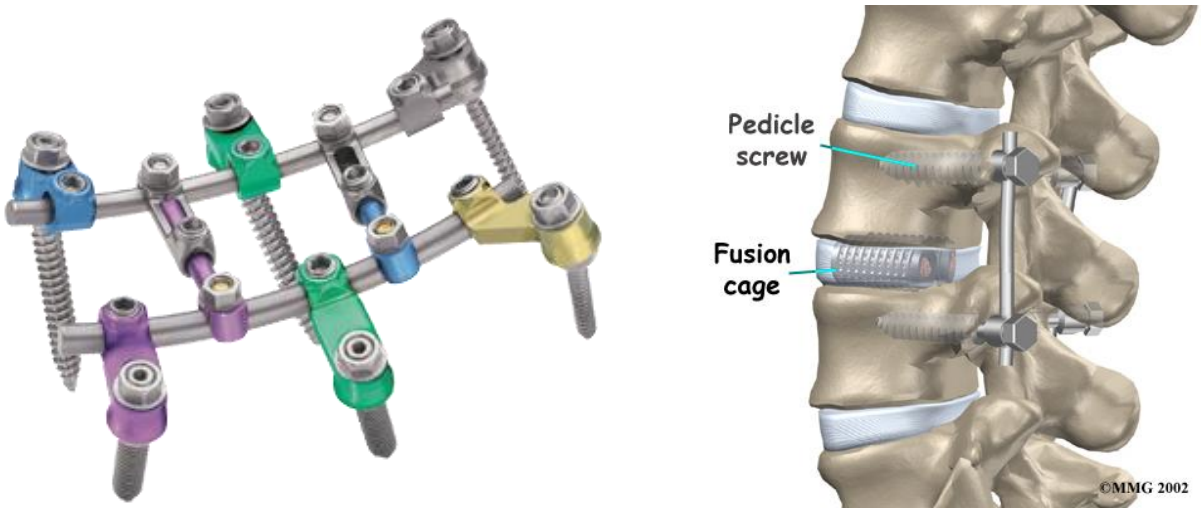

Figure 5: Spinal fixation device

In order to fit as much as possible the actual spine curvature of the patient, the rods must be bent, usually performing a three-point-bending, also called French bending. In consists positioning the rod between three pins – two lower support pins and one upper loading pin. The upper pin goes down applying the load set in input.

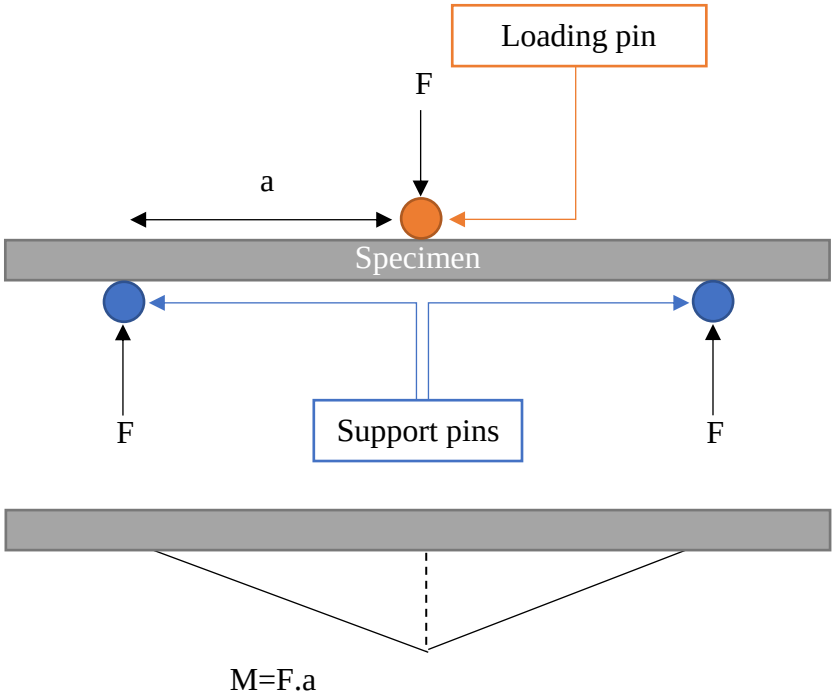

Figure 6: French bending set-up and bending moment graph

Table 2: Number of cycles and yield point [10]

Material	Load (N)	Number of cycles	Yield point
Stainless steel	250	2 000 000	
		2 000 000	
	300	2 000 000	
	400	1 018 774	Screw-rod interface
		248 681	Notch
		120 318	Screw head
	700	41 556	Notch
		35 868	Screw head
		25 675	Screw head
Ti6Al4V	250	479 702	Notch
		2 000 000	
	300	2 000 000	
	400	88 587	Notch
		73 903	Notch
		117 637	Notch
	700	13 960	Notch
		19 005	Notch
CoCrMb	250	2 000 000	
		2 000 000	
		2 000 000	
	400	782 714	Notch
		244 828	Notch
		325 529	Notch
	700	18 415	Screw head
		13 865	Screw head
		18 186	Screw head

Previous studies (see table 2) have shown that performing a French bending, both stainless steel and Cr-Co have failed after a higher number of cycles than Ti6Al4V. Moreover, while Ti6Al4V is more likely to have a notch failure, the failure is more in the screw region for Cr-Co.

However, other studies have demonstrated that Ti6Al4V remains a better choice in terms of biocompatibility since wear particles of Cr-Co can induce inflammation of the tissues close to the fixation after a long period [10].

Titanium rods in spinal surgery

Thanks to their adequate stiffness, yield, fracture and corrosion resistance, their excellent fatigue life, their high biocompatibility and the absence of MRI artifacts, titanium alloys usage in spinal surgery is increasing. Moreover, since its Young's modulus is lower than the one of other biocompatible materials, like stainless steel or cobalt-chromium alloys, titanium reduces the stress shielding effect. This phenomenon causes a higher stress distribution in the rod and induce a progressive bone resorption and embrittlement that leads to other pathologies in the bone close to the prosthesis.

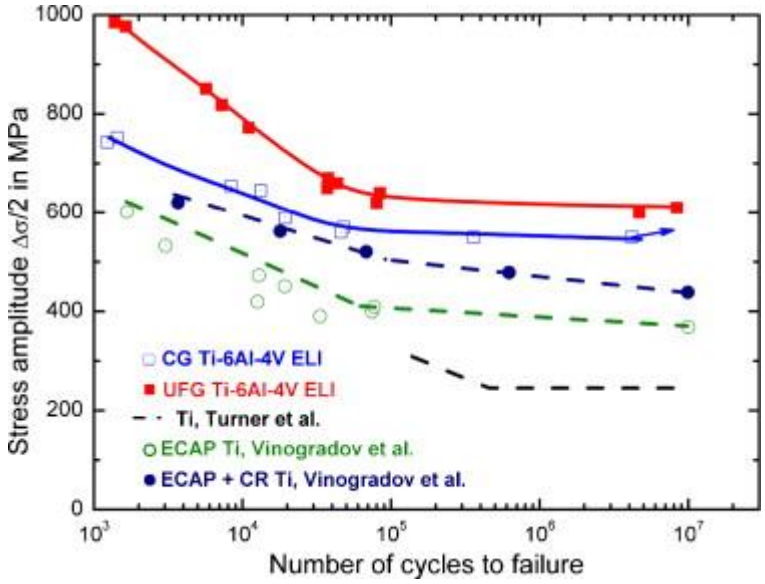

Figure 7: Titanium alloys Wöhler diagram [15]

However, titanium has shown a notch sensitivity. Indeed, all the manipulations performed by the surgeon, like the bending of the rod to fit to the patient anatomy or the use of screws create defects on the surface that would be the starting point for cracks propagation [14].

According to a study of Smith et al. [16], titanium rods are more likely to fail because of this notch sensitivity. Indeed, a multicentre, retrospective review of rod fracture was performed. 6.8% of the 442 patients analysed had symptomatic rod fracture, with a rate of failure equal to 8.6% for titanium.

Another study [17] has shown that, performing a four-point bending for 1 million cycles, while titanium rods with no notch did not failed, three titanium rods with a French bender notch (notch created after a French bending) with an average of 87,663 cycles. It constitutes a significant drop in fatigue life.

Fatigue

Principle

Fatigue is the weakening of a material caused by repeatedly applied loads. The nominal maximal stress that causes fatigue failure is lower than the yield stress of the material. During all the loading/release steps in which the material is subject, cracks start to appear in it. Once cracks reach a critical size, it propagates and failure occurs. However, by knowing the woheler diagram it is possible to have a statistical approach for an estimate of the fatigue behaviour.

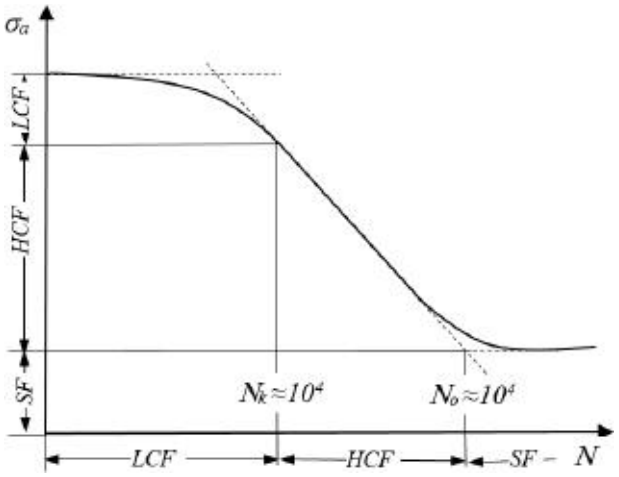

Figure 8: Example of a Wöhler diagram (SF: Safe Fatigue; HCF: High Cycle Fatigue; LCF: Low Cycle Fatigue; N: Number of cycles; σ_a: alternate stress)

Hence, for high values of stress, the fatigue phenomenon is a short term failure, while it is a long term failure for lower values of stress. Below a particular value, there is no failure due to fatigue (infinite life).

Assuming a cyclical solicitation of the material, four fundamental cases are possible

- Alternate symmetric;
- Alternate asymmetric;
- Oscillating from zero;
- Pulsatile.

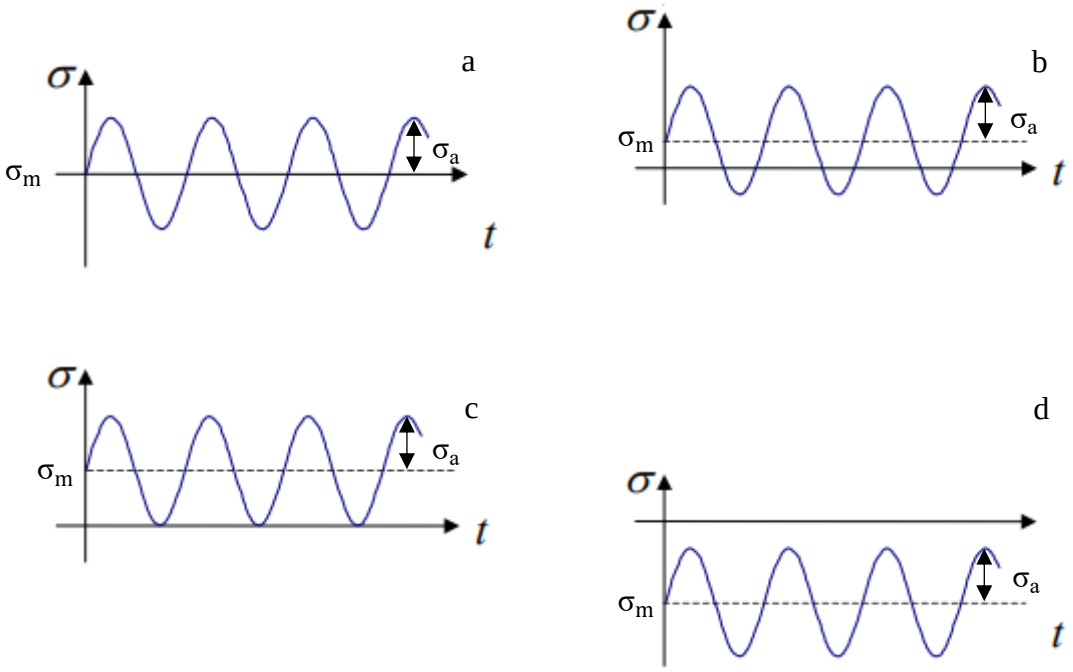

Figure 9: Four fundamental cases of cyclical solicitation (a: alternate symmetric; b: alternate asymmetric; c: oscillating from zero; d: pulsatile)

Since the fatigue implies sinusoidal loads, it is possible to define a mean and amplitude component of the oscillation, namely:

$$\sigma_m = \frac{\sigma_{max} + \sigma_{min}}{2}$$

and

$$\sigma_a = \frac{\sigma_{max} - \sigma_{min}}{2}$$

Knowing the value of the yield stress, the ultimate stress and the endurance limit of the material, the Goodman-Haigh diagram can also be plotted to determine the critical values of σ_m and σ_a for a fixed number of cycles.

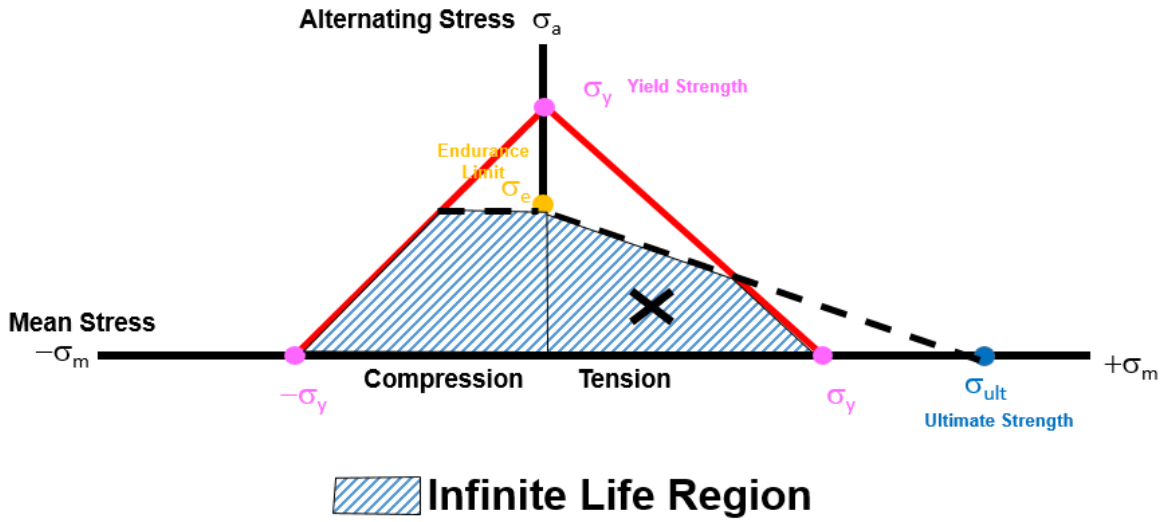

Figure 10: Goodman-Haigh diagram for infinite life

MESA Rail™ rod

This spinal rod is manufactured by the company K2M which is specialized in spine solutions. “The K2M MESA Rail™ is a new implant with a unique beam-like design which provides increased rigidity compared with a standard circular rod of equivalent diameter potentially allowing greater control and maintenance of correction” [11]. To improve mechanical properties and to have a surface finish, the rods are zirconia-glass blasted.

Figure 11: MESA Rail™ rod

In 2012, a study concluded that the K2M MESA Rail is “a powerful new implant design” which allows to correct complex spinal deformity, in particular kyphotic deformity, and normal thoracic kyphosis, particularly in idiopathic thoracic curves, which tend to be lordosing. This may prevent thoracic flat back and potential long-term sequelae.

However, even is the early results has demonstrated that that the safety and the effectiveness of the MESA Rail are equivalent to other posterior deformity correction implants on the market, further studies must be performed to ensure the validity of the results un long terms [11].

Shot peening and cavitation peening

In order to improve the fatigue strength of a material, a shot peening or a cavitation peening can be performed. Both techniques consist in introducing residual compressive stress near the surface. For shot peening, metallic, glass or ceramic spheres are usually used to impact to the surface of the rod and induce plastic deformation. For cavitation peening, the same effect is obtained thanks to high-speed water jet [12].

Experimental approach

It consists in performing a test that will involve bending properties of the rod, like the French bender or the four-point bending, to impose a loading and a release load and to count the number cycles the rod can bear before rupture. It is also important to know the value of the area of the section to be able to calculate the stress. This approach is the easiest to set-up but is also the most expensive. Indeed, to have relevant results, it is necessary to run a lot of identic experimental tests on the rods. Since the rod is broken at the end of a test, a consequent quantity of rods is needed.

Experimental tests were performed on glass zirconia blasted MESA Rail™ rods in 2017 at Politecnico di Milano [3], but on a small number of rods (a total of 7). The four-point-bending method was used, with a run-out of 10^6 cycles.

Numerical approach

It consists in the 3D reconstruction of the rod to simulate constraints on it and obtain results similar to an actual test. A finite element analysis is performed. Instead of studying a continuous volume, this latter is discretized into smaller volumes. All the variables of interest will be determined for those volumes. Those variables are constant into each volume. As for the experimental approach, tests like the French bender or the four-point bending have to be simulated.

The main issue with this kind of approach is the calculation power of the devices used. Indeed, to have reliable results, it is fundamental to well characterize the sample (material properties, shape, interaction properties with other bodies, etc).

The goal of this project is to obtain a CAD model of the MESA Rail™ rod in order to be able to interpret its fatigue phenomenon after 10^6 cycles.

Geometry

In this chapter will be detailed the steps to describe the rod and its shape, in order to prepare the CAD reconstruction of the MESA Rail™.

Measures

The MESA Rail™ dimensions were measured using a microscope during the previous work [3]. The results are reported in Table 1 (p 41 of the previous work [3]).

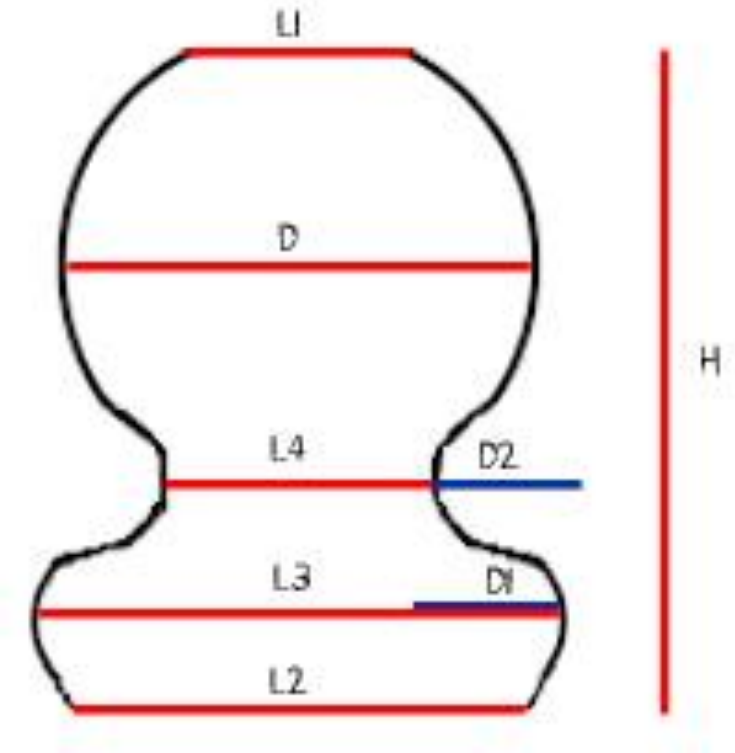

Figure 12: Section with dimensions names

Table 3: Useful values to draw the MESA Rail™ section from the previous work [3]

Distance	Mean value (mm)	Standard deviation (%)	Variation (%)
Diameter (D)	4.35	4%	0.83%
Total high (H)	5.52	3%	0.57%
Upper base (L1)	1.69	3%	1.85%
Lower base (L2)	3.64	3%	0.86%
Diameter lower circles (D1)	1.08	10%	9.36%
Diameter external circles (D2)	1.09	4%	3.33%
Distance lower circles (L3)	4.20	3%	0.75%
Distance external circles (L4)	2.45	3%	1.28%

Drawing the rod section

To obtain the model in Abaqus, its section must be sketched with the dedicated tool. The 8 steps to get the final section are described in Figure 13. The useful values are the ones reported in Table 3 and 4.

Step 1:

- Draw a circle with diameter D.

Step 2:

- Trace two horizontal chords of the circle with length L1;
- Remove the external parts of the circle.

Step 3:

- Extend the lower line of a length X1 on each side.

Step 4:

- Draw the eternal circles with diameter D2, centered on the endpoints of the lower line.

Step 5:

- From the center of the external circle, trace a vertical line of length Y2;
- From the endpoint of this line, trace a horizontal line of length X2;
- Draw the lower circle of diameter D1, centered on the endpoint of the previous line.

Step 6:

- Trace the lower vertical radius of the lower circle;
- Draw the lower base of length L2, connecting the bottom extremity of the radius previously traced;

- Trace the tangent of the lower circle passing through the endpoint of the lower base.

Step 7:

- Using the tool “Create Spline: Thru Points” in the sketching module, connect the 5 following points:
  - The two intersections between the external circle and the main circle;
  - The two intersections between the external circle and the lower circle;
  - The intersection between the lower circle and its tangent;
- Remove the part of the previous curve between the two last points, the external circle, the inner lines, the lower part of the main circle and the inner part of the lower circle.

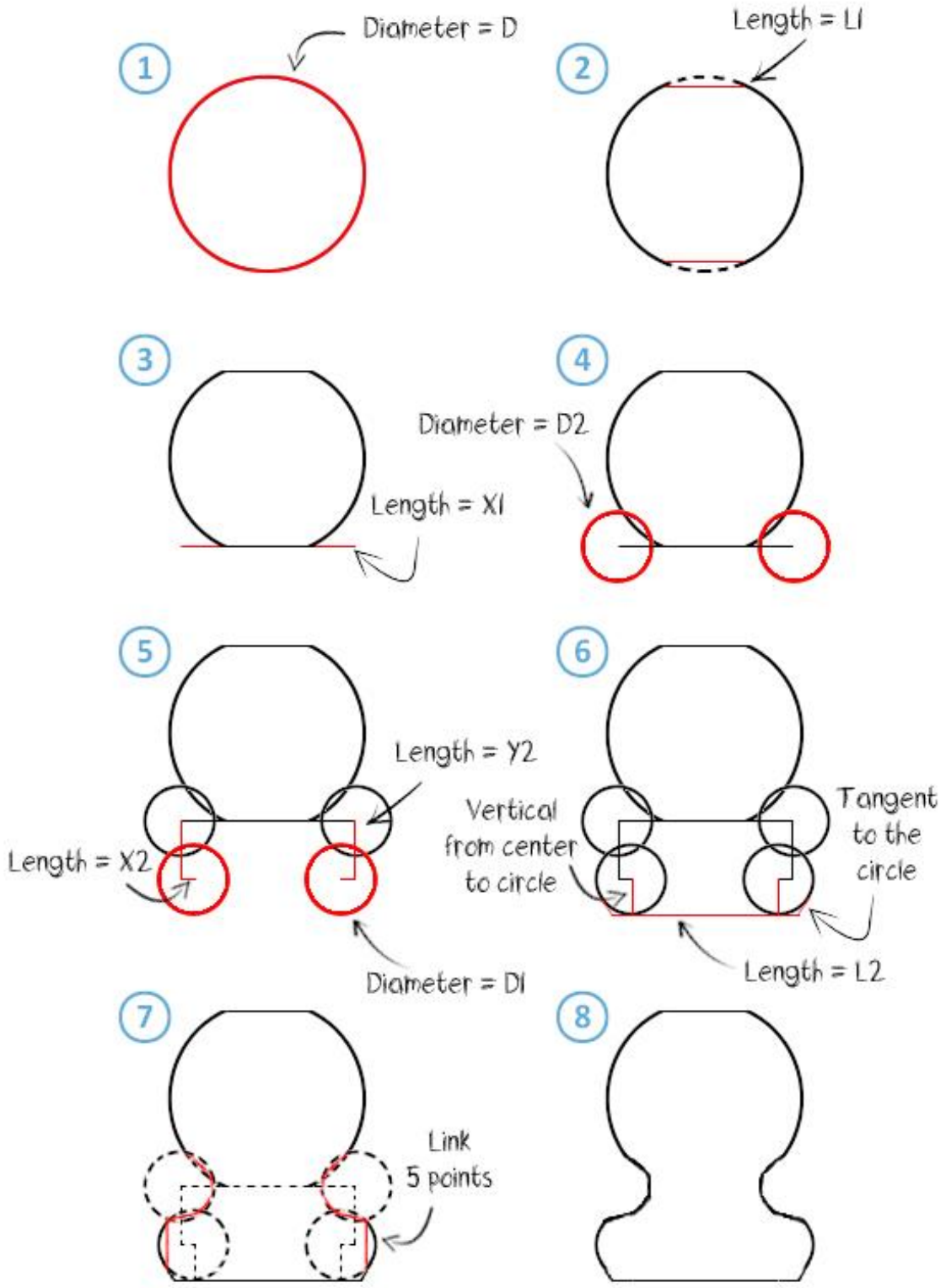

Figure 13: Steps to sketch the MESA Rail™ section

To sketch the section, three other values must be used: X1 (Figure 13 – step 3), X2 (Figure 13 – step 5) and Y2 (Figure 13 – step 5), and another value Y1 (Figure 14) is needed to calculate Y2. Those values can be obtained with the following equations:

- $X1 = \frac{L4-L1}{2} + \frac{D2}{2}$ (1)
- $X2 = \frac{L4-L3}{2} + D2$ (2)
- $Y1 = \frac{D}{2} - \sqrt{\left(\frac{D}{2}\right)^2 - \left(\frac{L1}{2}\right)^2}$ (3)
- $Y2 = H - D - \frac{D1}{2} + 2.Y1$ (4)

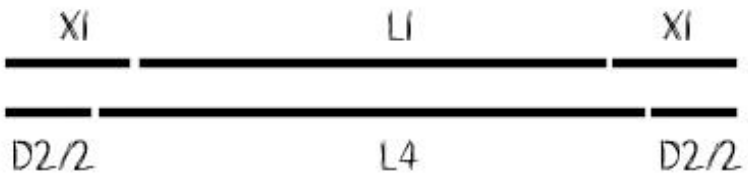

$$2.X1 + L1 = D2 + L4$$

$$\rightarrow X1 = \frac{L4 - L1}{2} + \frac{D2}{2}$$

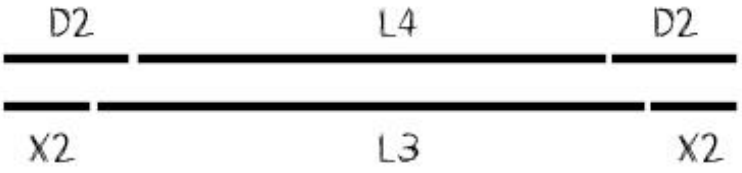

$$2.X2 + L3 = 2.D2 + L4$$

$$\rightarrow X2 = \frac{L4 - L3}{2} + D2$$

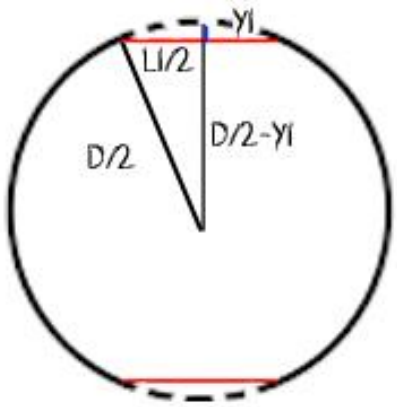

$$\left(\frac{D}{2}\right)^2 = \left(\frac{L1}{2}\right)^2 + \left(\frac{D}{2} - Y1\right)^2$$

$$\rightarrow Y1 = \frac{D}{2} - \sqrt{\left(\frac{D}{2}\right)^2 - \left(\frac{L1}{2}\right)^2}$$

Figure 13: relevant distances to calculate Y1

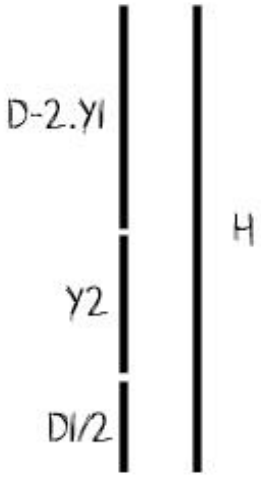

$$D - 2.Y1 + Y2 + \frac{D1}{2} = H$$

$$\rightarrow Y2 = H - D - \frac{D1}{2} + 2.Y1$$

$$\rightarrow Y2 = H - D - \frac{D1}{2} + D - 2.\sqrt{\left(\frac{D}{2}\right)^2 - \left(\frac{L1}{2}\right)^2}$$

The results are reported in table 3:

Table 3: Useful values to draw the MESA Rail™ section obtained from calculation

Distance	**Mean value (mm)**
Distance from the main circle to the center of the external ones (X1)	0.925
Horizontal projection of the distance between the centers of the circles (X2)	0.26
High of the removed upper part of the circle (Y1)	0.17
Vertical projection of the distance between the centers of the circles (Y2)	0.97

Abaqus

To get the CAD reconstruction of the MESA Rail™ and to perform the calculations, the software used has the following specifications:

- Name: Abaqus;
- Module: Abaqus CAE;
- Developer: Dassault Systèmes;
- Version used: 2018;
- System: Microsoft Windows;
- Function: creation of 2D and 3D designs.

In order to reduce the computational time, due to the symmetries of the problema a quarter of the rod can be considered. Hence, once the section is sketched, half of it can be removed and the extrusion will be only on 50mm instead of 100mm. Using symmetry plans, it is then possible to obtain the results as if the calculation were run of the complete rod.

Once the section is sketched in Abaqus, it is extruded about 50mm to obtain the following model figure 14.

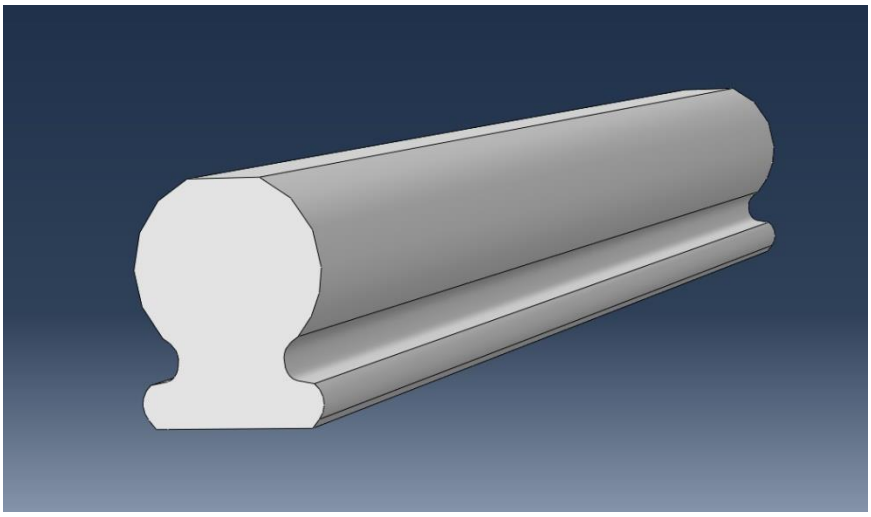

Figure 14: Extruded bar in Abaqus with full section

As previously mentioned, the calculation will be run only on half of the section, wich leads to the model figure 15.

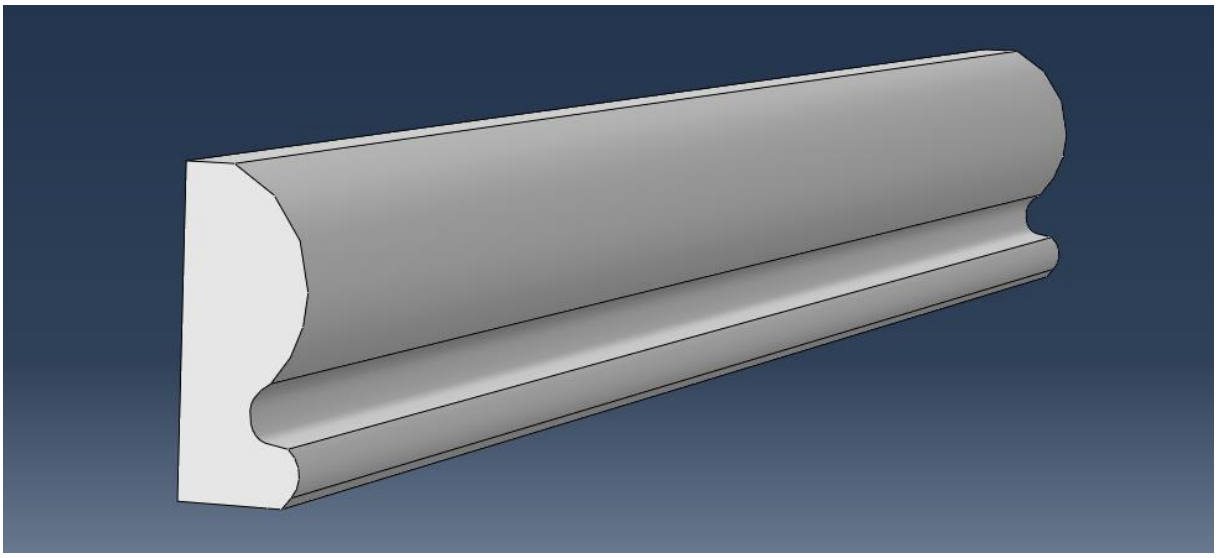

Figure 15: Extruded bar in Abaqus with half of the section

The section is then partitioned, in order to have a regular mesh and then to get reliable results. An example of a partition that leads to an acceptable meshing is presented figure 16.

Figure 16: Partitioned section

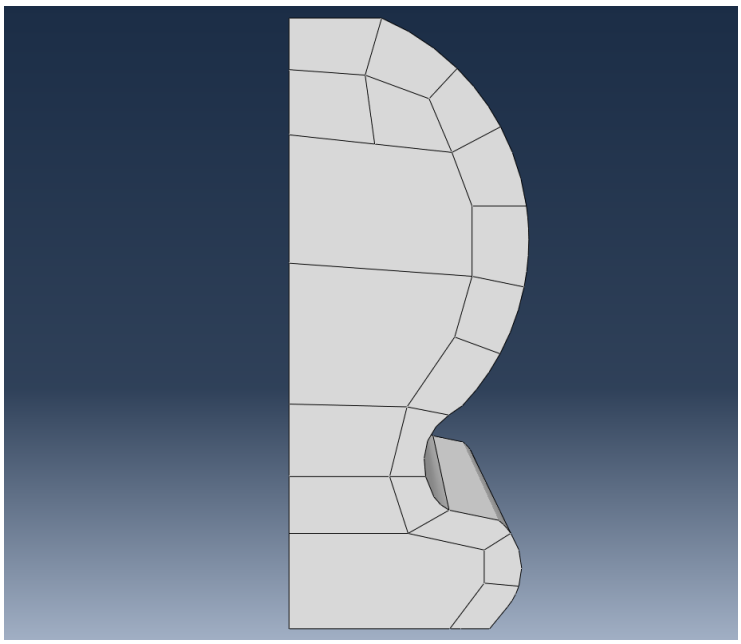

The pins

Two identic pins are also modelized and extruded over 3mm. Figure 17 and 18 present the pins and how they are disposed regarding the rod.

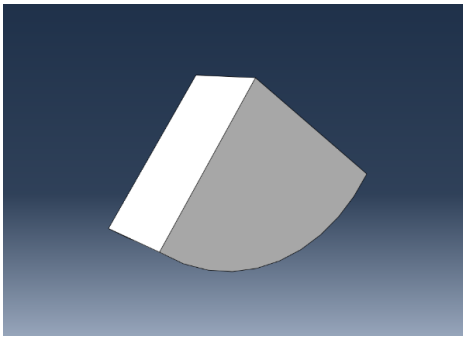

Figure 17: Extruded pin

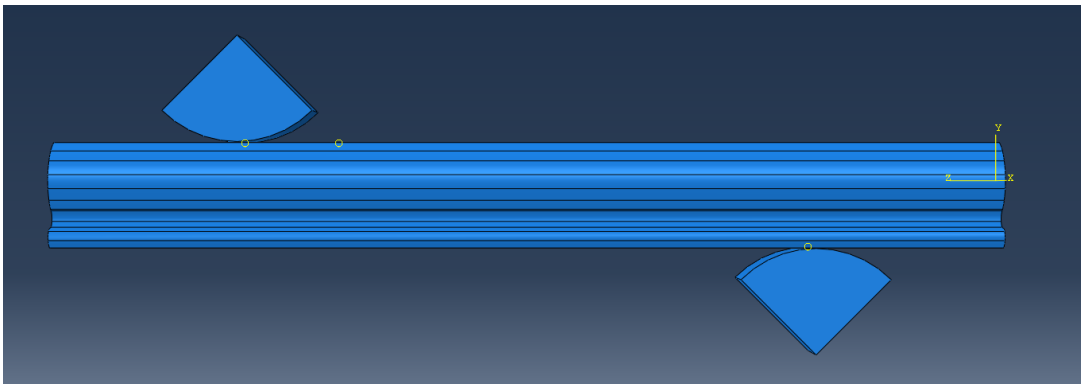

Figure 18: Disposition of the pins regarding the rod (symmetry plan on the left)

Mesh

This chapter will deal with the meshing of the rod volume in order to perform a finite element analysis. Particularly, a comparison between different meshes of different qualities will be performed.

Mesh sensitivity

Since finite not-convergent mesh may introduce errors in the calculation, it is fundamental to perform a mesh sensitivity: this has been done by creating three different mesh refinements – a coarse mesh, an intermediate mesh and a fine mesh. The comparison in terms of force-displacement curves and maximum principal stress allowed the choice of the best refinement, as a trade off between computational cost and accuracy. It was chosen a 5% error as a limit threshold for convergence

In this part, the distance between the two upper pins is set at 30mm while the distance between the bottom ones is set at 80mm and the friction factor between the rod and the pins is set at 0,175 [2]. During the loading step, a displacement of 7 mm is applied on the upper pin. Then, there is a release step during which the pin goes back to its initial position.

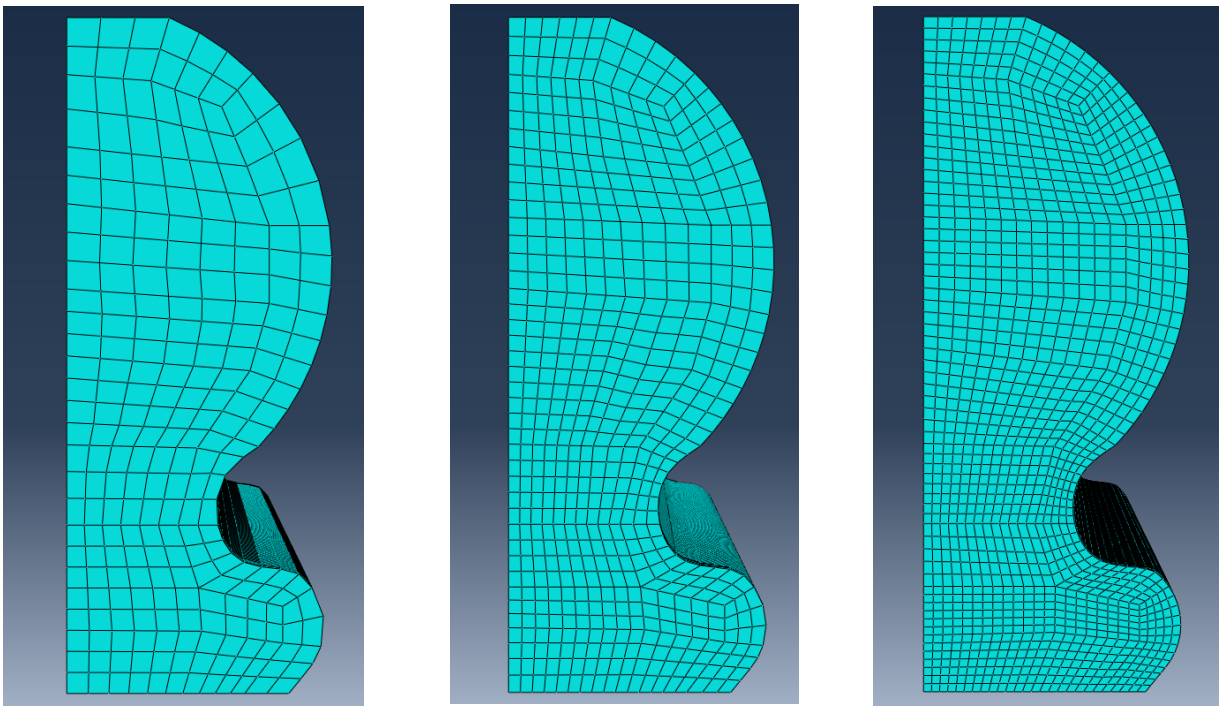

Figure 19: Coarse mesh (left), intermediate mesh (middle) and fine mesh (right)

Three different element types are also compared for each mesh refinement: full integration solid elements (C3D8), reduced integration solid elements (C3D8R) and full integration incompatible mode solid elements (C3D8I). Theorethically, the C3D8R allows to

have the fastest calculations with less accuracy while the full integration incompatible mode type allows calculations faster than the normal type but with good accuracy for bending.

Four-point bending

The test that will be simulated is the four-point bending. In this configuration, two support pins are encastered while two loading pins are moving down and are bending the specimen. It allows to have a constant bending moment in the gauge length (distance between the two upper pins).

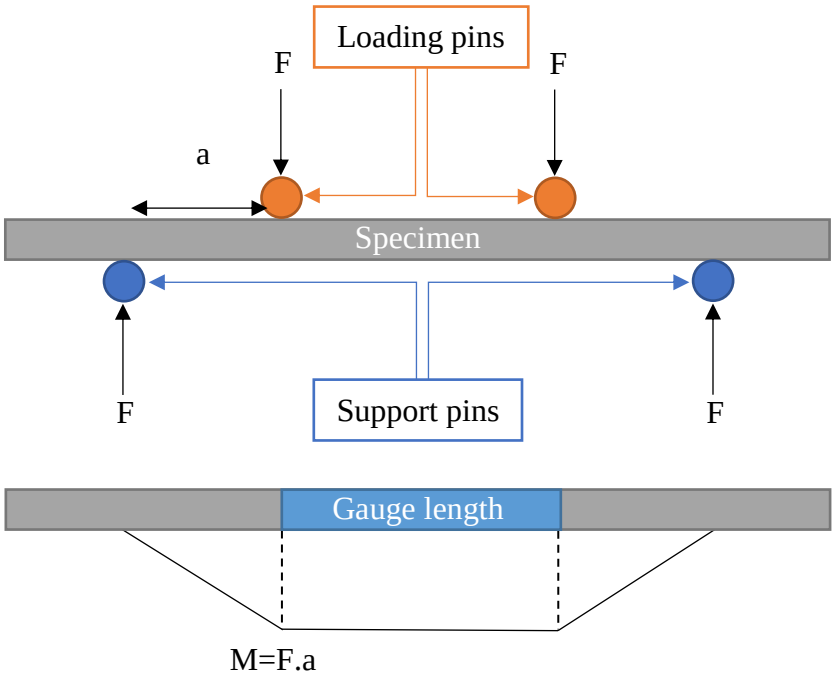

Figure 20: Four-point bending set-up and bending moment graph

Mesh choice

Using the settings previously mentioned, the following shapes for the rod are obtained in Abaqus for the coarse mesh using C3D8I element type, at the end of the loading step and at the ending of the release step. The 8 other results are similar to this one.

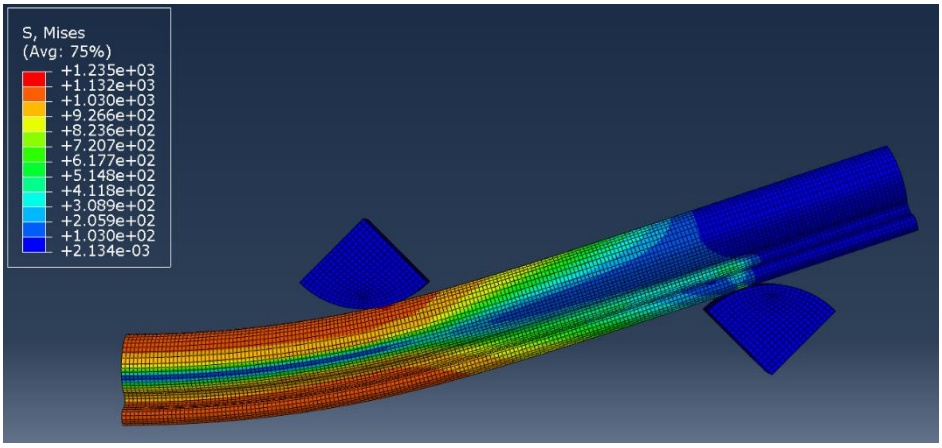

Figure 21a: MESA Rail™ in Abaqus at the end of the loading step, coarse mesh C3D8I

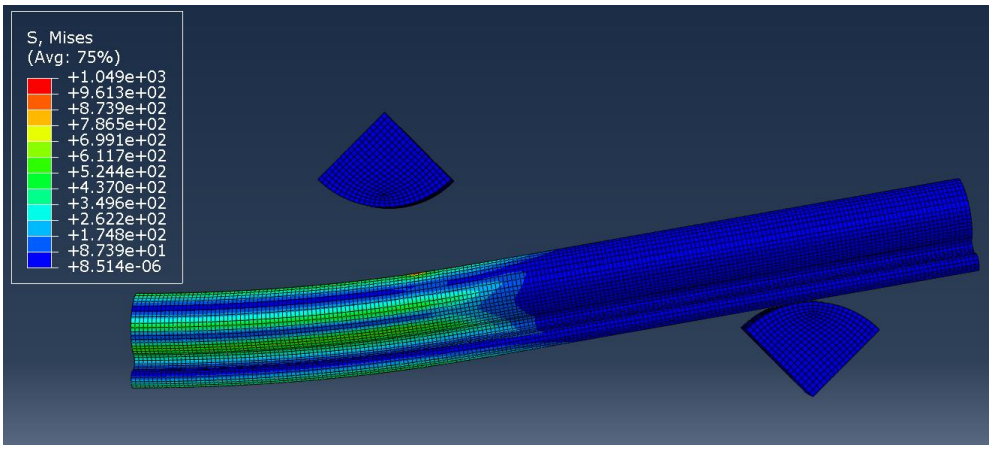

Figure 21b: MESA Rail™ in Abaqus at the end of the release step, coarse mesh C3D8I

The reaction force on the support pin and the displacement of the loading pin are then extracted and processed in an Excel file in order to obtain the following reaction force/displacement graphs. Since the analysis in Abaqus is just on a quarter of the rod, the reaction force extracted has been multiplied by 4.

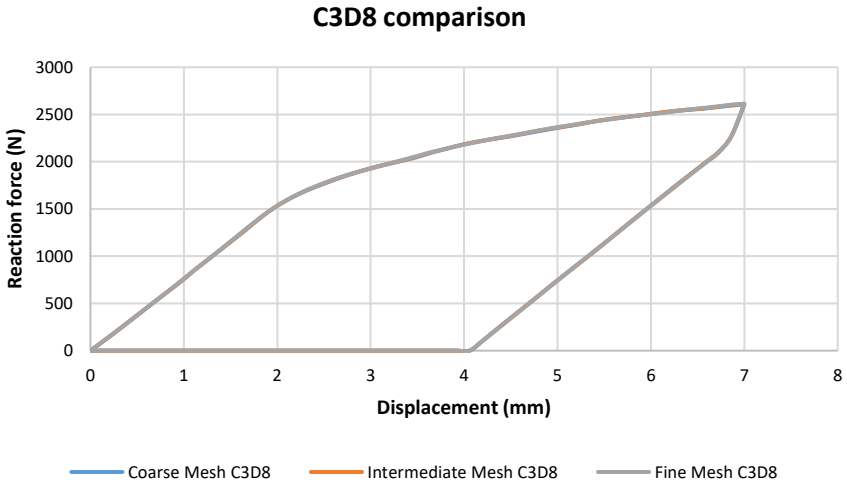

Figure 22a: Mesh comparison using the full integration element formulation

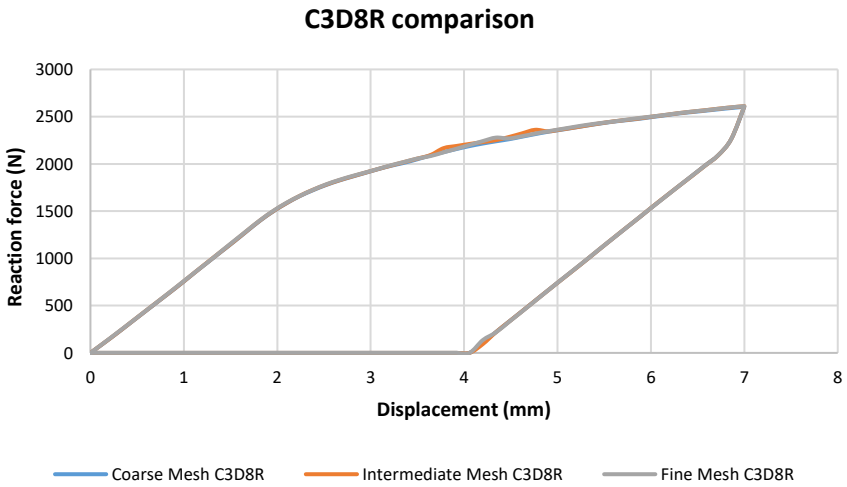

Figure 22b: Mesh comparison using the reduced integration element formulation

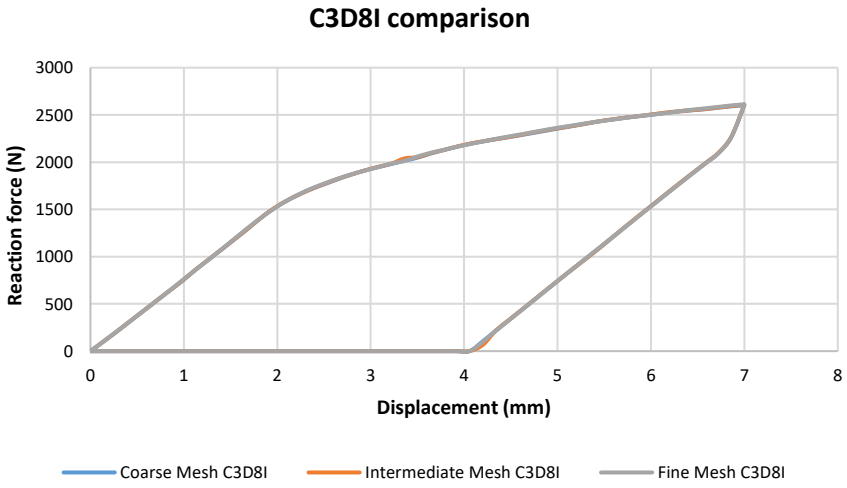

Figure 22c: Mesh comparison using the full integration incompatible mode element formulation

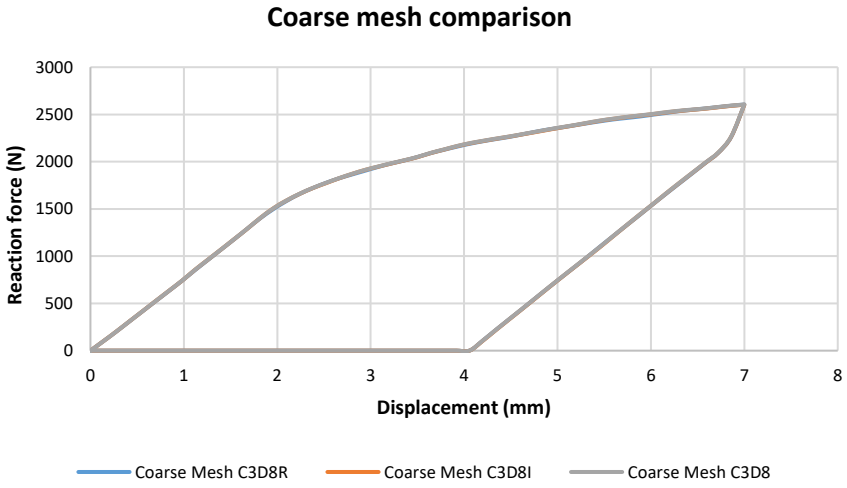

Figure 23a: Element formulation comparison using the coarse mesh

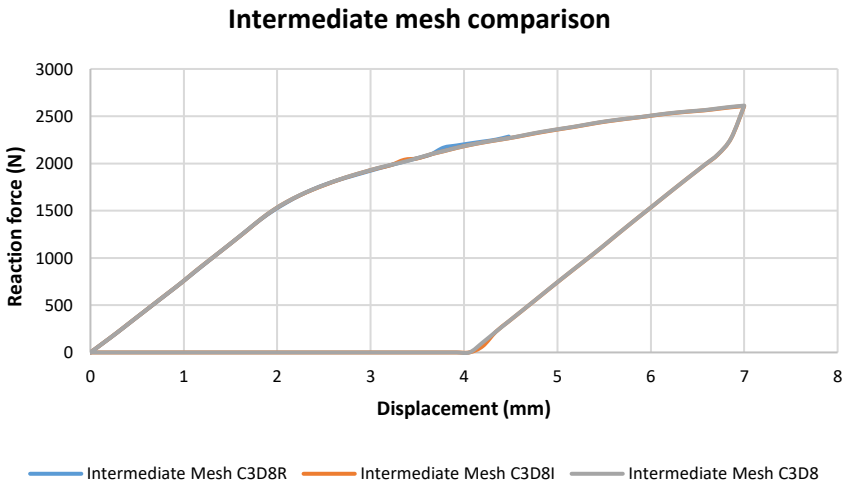

Figure 23b: Element formulationcomparison using the intermediate mesh

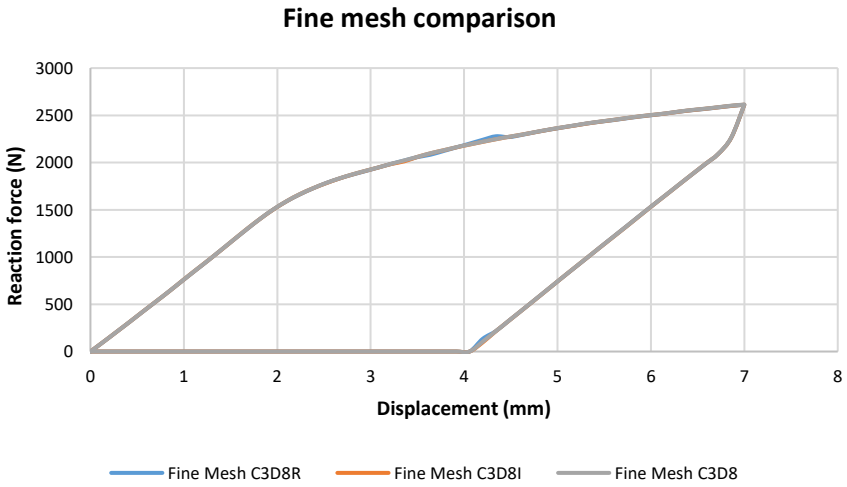

Figure 23c: Element type comparison using the fine mesh

From these global variables, a first conclusion is that there is no difference according to the mesh used and the element type used. As a consequence it was chosen to use the C3D8I element formulation, since the computational time is almost equivalent and it gives the best accuracy in treating bending dominated problems, as underlined on figure 24. The results are reported table 5.

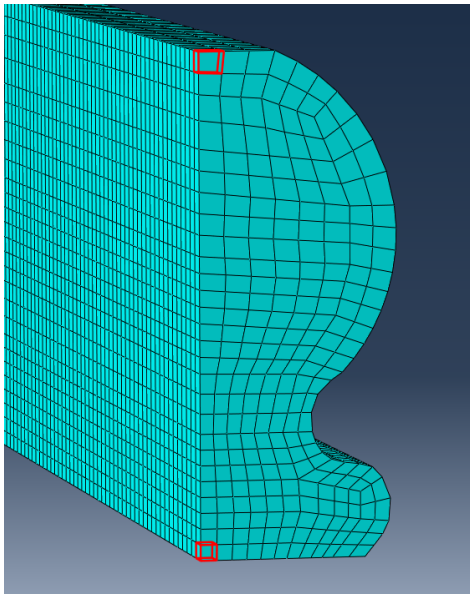

Figure 24: Coarse mesh with interest volumes in red

Table 5: Comparison of the maximum principle stress according to the mesh used

Mesh	Step	Element	Max Abs (MPa)	Comparison to Fine (%)
Coarse	Bending	Top	-1112,81	0,008
		Bottom	1116,10	0,039
	Release	Top	389,06	4,052
		Bottom	-372,18	1,991
Intermediate	Bending	Top	-1111,76	-0,085
		Bottom	1116,85	0,106
	Release	Top	365,84	-2,157
		Bottom	-378,78	3,799
Fine	Bending	Top	-1112,71	
		Bottom	1115,66	
	Release	Top	373,91	
		Bottom	-364,91	

Since the differences between the results on the coarse mesh and on the fine mesh are less than 5%, it is possible to conclude that the coarse mesh gives good approximations of the actual behaviour of the rod under four-point bending. It was chosen as the convergent refinement for the further analysis.

The expected behaviour during a four-point bending is also observed. The loading step exhibits the typical tension-compression gradient due to pure bending in the rod. Since the local values of stress are overcoming the yielding threshold, it is expected to have residual stress. This explains why at the release the state of stress is inverted [1].

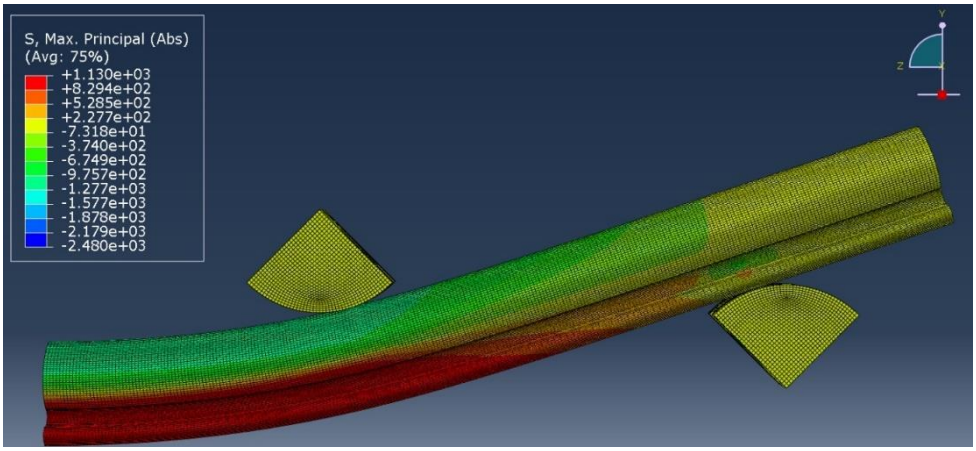

Figure 25: Maximum principal stress at the end of the bending step (fine mesh, C3D8I)

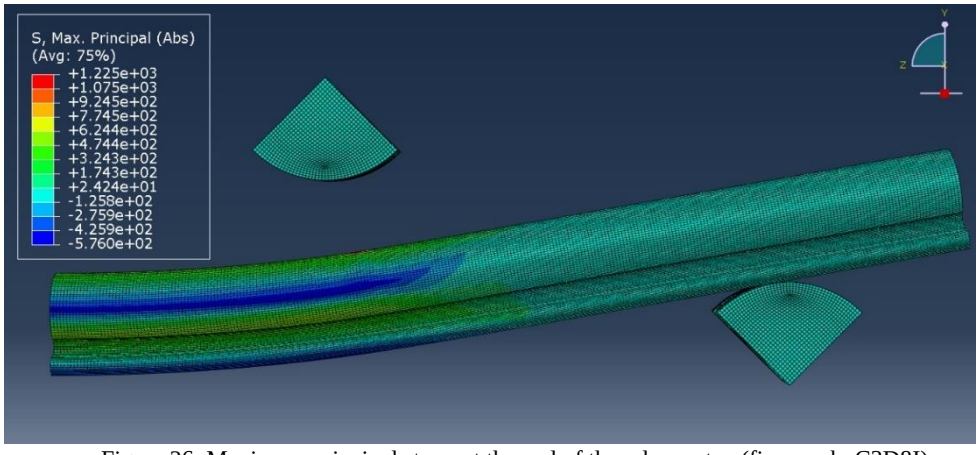

Figure 26: Maximum principal stress at the end of the release step (fine mesh, C3D8I)

Material properties

In this chapter will be defined the material properties of the rod and a friction sensitivity will be run to fit as much as possible to the actual rod.

Material definition

The material of the actual rod is a titanium but since no exact information on it is available, the material used for the rod is a standard titanium alloy which properties were figured out with tests performed on circular rods (manufactured by the same company) in a previous work [1]. Hence, the Young's modulus is 110GPa, the Poisson's ratio is 0.3 and the plastic behaviour is set according to the following table.

Table 6: Material plastic behaviour

Yield stress (MPa)	Plastic strain (-)
885.7366288	0
920.1149504	0.001836946
967.5849306	0.005744008
1026.247377	0.010132048
1065.545573	0.014754124
1088.254278	0.017919715
1107.217369	0.025970282
1125.689174	0.035990449
1133.867074	0.049977428

The material chosen for the pins is a linear elastic stainless steel with a Young's modulus equal to 210GPa and a Poisson's ratio equal to 0.3. The elasticity assumption is a strong one, but it has been proven it does not affect the calculation [1].

Friction sensitivity

In literature, the friction factor for a stainless steel-titanium contact is usually set at 0.36. However, during a former work [1], a factor of 0.175 was estimated, allowing for the possible rotation of the pins during the test. It is then necessary to perform a friction sensitivity to try to fit to the experimental data as much as possible. The same test will be run but changing the friction factor that can be equal to 0.36 or 0.175. It will also be run in the frictionless case, since in theory there is no friction loading with circular pins.

In this part, the distance between the two upper pins is set at 30mm while the distance between the bottom ones is set at 80mm. As for the mesh sensitivity, the loading displacement is set at 7 mm and the pin goes back to its initial position at the end of the release step. The mesh refinement is the coarse one.

As for the mesh sensitivity, the reaction force/displacement curves are plotted figure 27 using the data extracted from Abaqus and compared to the experimental curve plotted using results from the previous work [3].

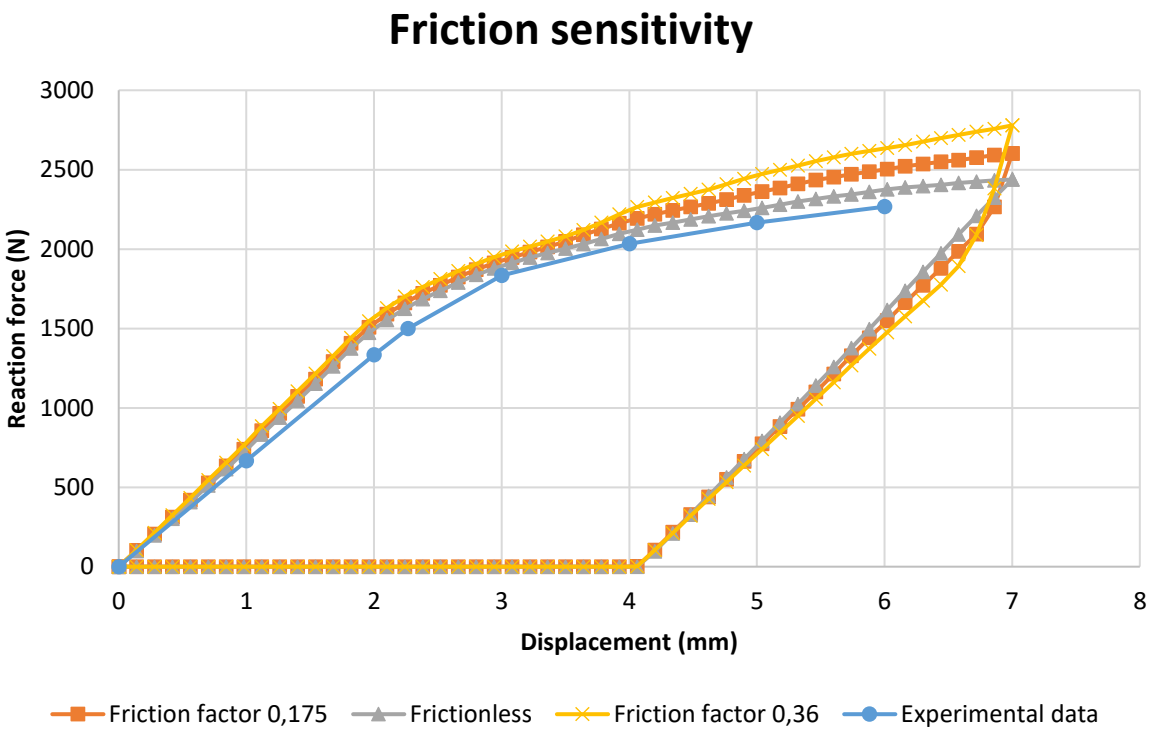

Figure 27: Reaction force(N)/displacement(mm) graph for friction sensitivity

The best fit is reached with the frictionless curve, while it was expected to get it with the friction factor equal to 0.175. It might be because the material properties used in Abaqus are not exactly as the same as the actual ones. However, since no complete data is available, particularly regarding the plastic behaviour, the best way to reach a good fit is to vary the friction factor. The further analysis will then be run in a frictionless case.

Fatigue analysis

In this chapter will be described the set-up of the experimental tests run previously [3] and the set-up of the numerical tests. Then, their results will be compared.

Experimental fatigue tests

Six fatigue tests were performed during the experimental tests [3], with six different loads for bending and release (indeed, ate the end of the release, the upper pin is not back to its initial position but continue to apply a smaller load on the rod). The loads applied were:

- Phase 1: 114/1140N;
- Phase 2: 133/1330N;
- Phase 3: 200/2000N;
- Phase 4: 170/1700N;
- Phase 5: 140/1400N;
- Phase 6: 160/1600N.

The distance between the two upper pins was 20 mm to avoid the stress intensification effects resulting from loading-pin indentation induced during the previous static step on UC rods [2], while the distance between the bottom ones is set at 80mm.

The tests ended with the following results:

- 114/1140N: Run out after 2.5 million of cycles;
- 133/1330N: Rupture after 1.10^5 cycles and 6.10^5 cycles;
- 200/2000N: Rupture after 8568 cycles;
- 170/1700N: Rupture after 47951 cycles;
- 140/1400N: Run out after 2.5 million of cycles;

  Since 133/1330N has failed, the rod was expected to fail in this case too. This brings to light that those cases are limit cases.
- 160/1600N: Rupture after 98206 cycles.

Those results allow to plot a draft Wöhler diagram.

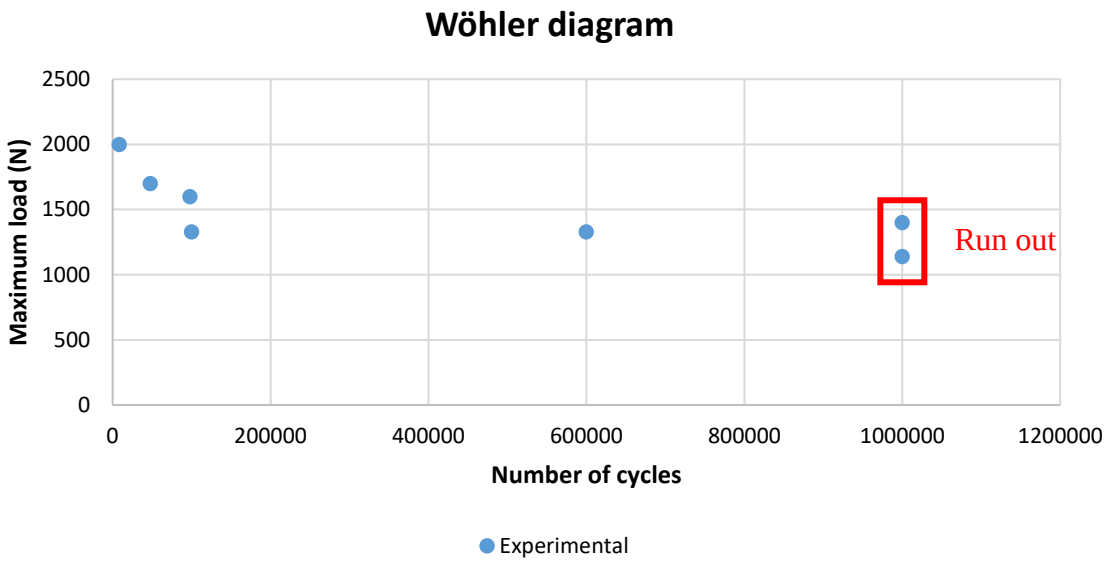

Figure 28: Wöhler diagram guessed after the experimental tests [3]

MATLAB R2018a

The software MATLAB R2018a will be used to postprocess 10^6 cycles of loading/release from the results in Abaqus with 3 cycles.

- Name: MATLAB R2018a;
- Developer: Mathworks;
- Version used: 2018;
- System: Microsoft Windows;
- Function: programming software.

Numerical fatigue tests

Six simplified simulations are run during 3 cycles of loading and release, using as the same loads as for the experimental tests.

In this part, the distance between the two upper pins is set at 20mm, while the distance between the bottom ones is set at 80mm. As concluded in the previous part, the mesh used is the coarse one, the element type in the full integration incompatible mode type and there is no friction factor.

To have an easier convergence of the implicit solver, a displacement is applied on the pins, and not a load. It is then necessary to calibrate the analysis finding the right displacements for each phase, in order to have the desired load. Using the results of a fatigue test with the same set-up but with a displacement equal to 7mm and a complete release (return to the initial point), the displacements to use for the six phases is figured out on Excel, predicting a linear behaviour. Then, after one run with these advised displacements, they are adjusted using the same method until having a reaction force equivalent to the target load (with a 5% tolerance).

Once the displacements are determined, the same tests are run for 3 cycles of bending/release and the stress tensors at the end of the third bending and at the end of the third release within the gauge length are extracted and computed in MATLAB R2018a, using a script written for the previous work [2]. Thanks to this script, 10^6 cycles are postprocessed and constant life diagrams are plotted.

The results of the calibration step are reported on table 7.

Table 7: Calibration of the analysis for the frictionless case

		Phase 1	Phase 2	Phase 3	Phase 4	Phase 5	Phase 6
Target (N)	Fmax	1140	1330	2000	1700	1400	1600
	Fmin	114	133	200	170	140	160
FEA (N)	Fmax	1139.80	1330.82	2000.05	1700.13	1400.85	1600.38
	Fmin	113.99	133.07	200.02	169.88	139.76	160.28
Error (%)	Fmax	0.02	-0.06	0.00	-0.01	-0.06	-0.02
	Fmin	0.01	-0.06	-0.01	0.07	0.17	-0.17
Displacement (mm)	After loading	1.903	2.28	8.24	3.904	2.476	3.291
	After release	0.206	0.329	5.383	1.462	0.425	0.98

Then, the simulations on 3 cycles are run, using the values defined by the calibration step and the following constant life diagrams are plotted thanks to the MATLAB script. As explained in the previous work [2], "the stress components were combined according to the Sines' criterion, recommended for Titanium alloys and metals in general (5)

$$\sigma_{SINES} = \sigma_{VM,a} + K * I_m$$

where the alternate component of the von Mises stress ($\sigma_{VM,a}$) and the average component of the hydrostatic stress (I_m) were calculated as follow:

(6)

$$\sigma_{VM,a} = \sqrt{\frac{1}{2}\left[\left(\sigma_{1,a} - \sigma_{2,a}\right)^2 + \left(\sigma_{1,a} - \sigma_{3,a}\right)^2 + \left(\sigma_{2,a} - \sigma_{3,a}\right)^2\right]} \quad (7)$$

$$I_m = \sigma_{1,m} + \sigma_{2,m} + \sigma_{3,m} = 3P_m$$

where $\sigma_{1,m}$, $\sigma_{2,m}$, $\sigma_{3,m}$ are the mean principal stresses, $\sigma_{1,a}$, $\sigma_{2,a}$, $\sigma_{3,a}$ are the alternate principal stresses – namely the eigenvalues of the mean and alternate stress tensors respectively – and P_m is the hydrostatic pressure. Mean and alternate stresses tensors were computed from the principal stress tensors at fatigue peak and valley as

$$\sigma_{ij,m} = \frac{\sigma_{ij}{}^{peak} + \sigma_{ij}{}^{valley}}{2} \tag{8}$$

$$\sigma_{ij,a} = \frac{\sigma_{ij}{}^{peak} - \sigma_{ij}{}^{valley}}{2} \tag{9}$$

In Eq. (5), the K parameter can assume a range of values dependent on the material grain size and surface roughness; K is defined by the ratio $\frac{\sigma_{FA,f}}{\sigma_R}$, where σ_R is the material ultimate strength as obtained in tensile tests, while $\sigma_{FA,f}$ indicates the maximum alternating load resulting in infinite fatigue life for $R = -1$. For Ti6Al4V, a reasonable value could be set between 0.5 and 0.7, and the distribution of Sines equivalent stress will be displayed assuming $K = 0.5$."

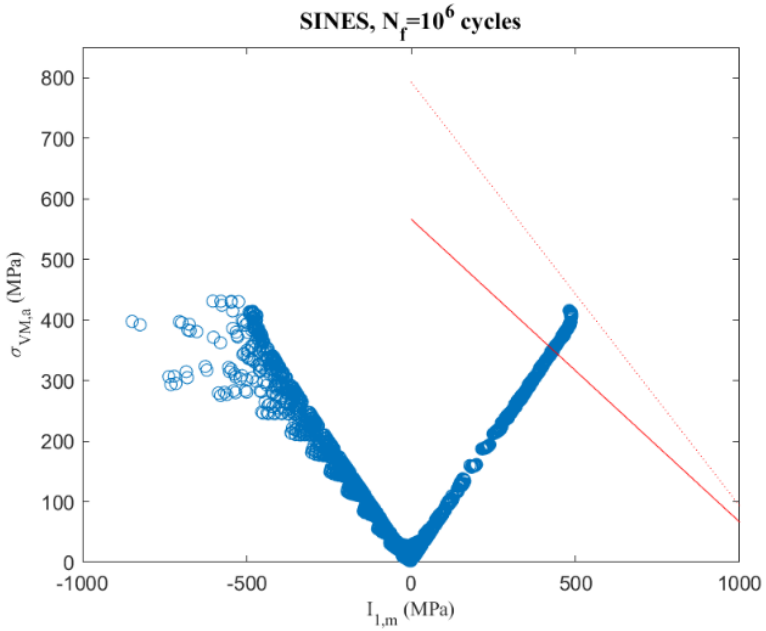

Figure 29a: Constant life diagram for Phase 1

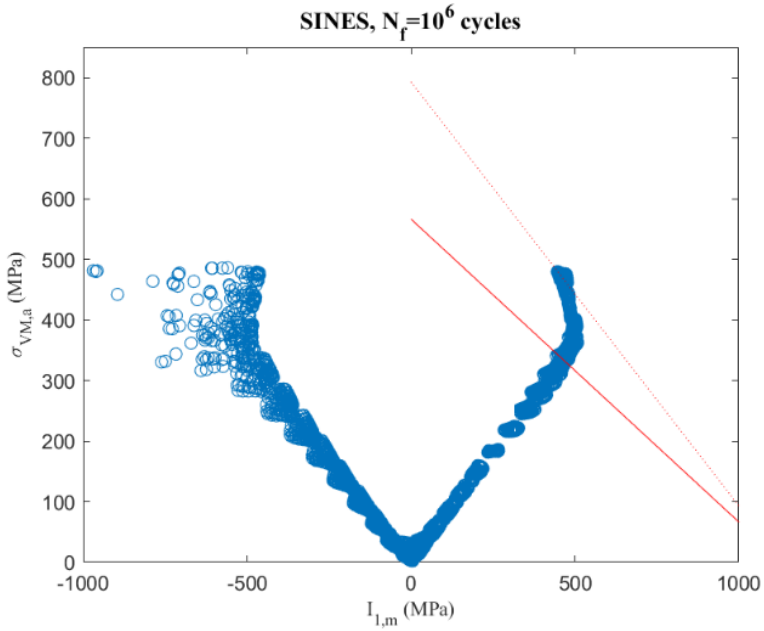

Figure 29b: Constant life diagram for Phase 2

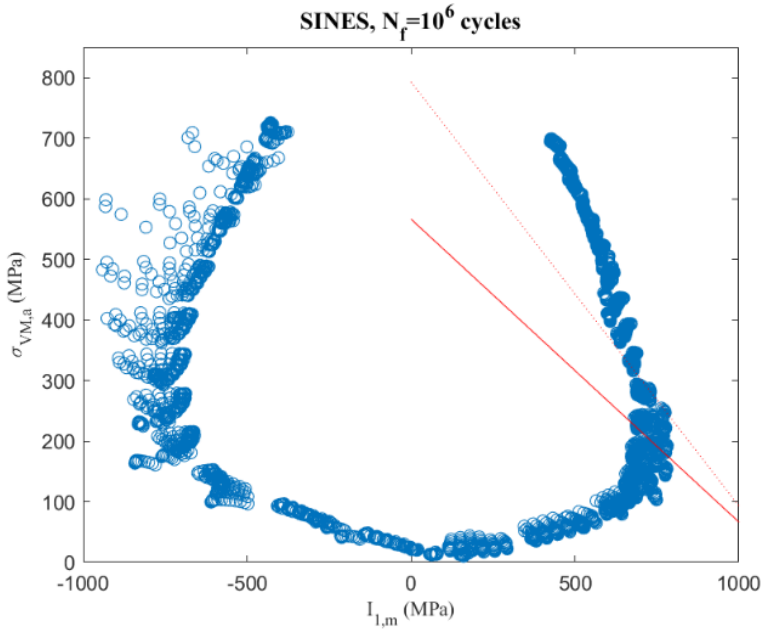

Figure 29c: Constant life diagram for Phase 3

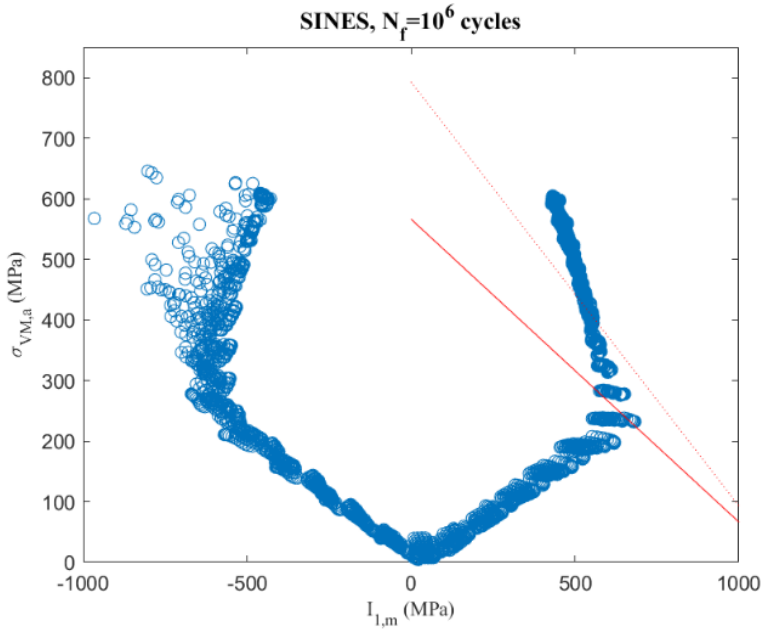

Figure 29d: Constant life diagram for Phase 4

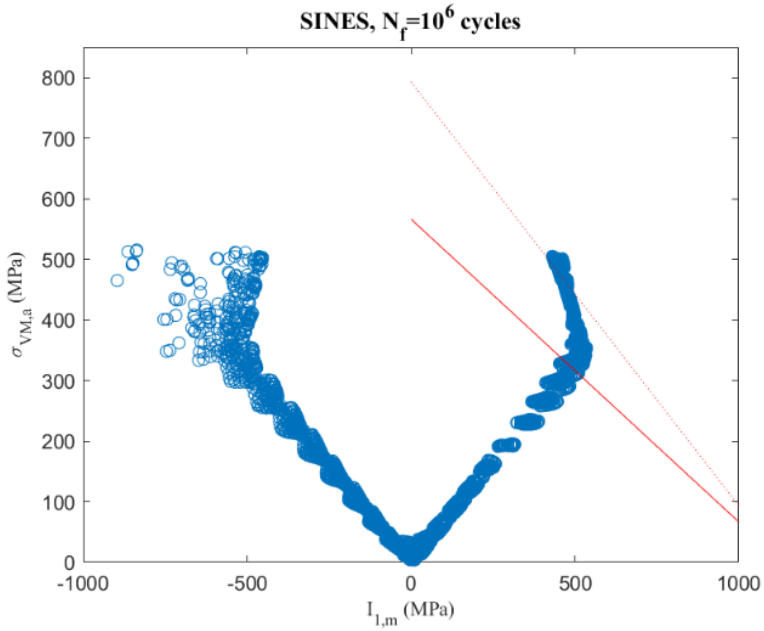

Figure 29e: Constant life diagram for Phase 5

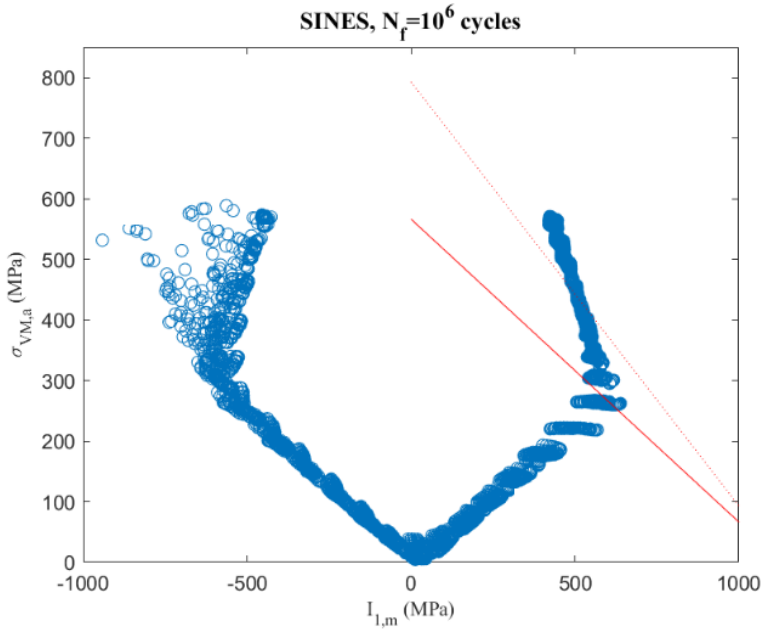

Figure 29f: Constant life diagram for Phase 6

From those diagrams, the fatigue behaviour of the rod can be figured out:

- 114/1140N: Run out

  The diagram does not cross the K=0.7 curve and is quite "far" of it, so the rod is not expected to break;

- 133/1330N: Limit case

  The diagram's end is on the K=0.7 curve, so the rod can break after a lot of cycles or never break;

- 200/2000N: Rupture

  The diagram clearly crosses the K=0.7 curve, the rod will break before the 10^6 cycles;

- 170/1700N: Rupture

  As same conclusion as 200/2000N case;

- 140/1400N: Limit case

  As same conclusion as 133/1330N case;

- 160/1600N: Rupture

  As same conclusion as 200/2000N case.

Those results are consistent with the experimental results. Indeed, it confirms the results for phases 1, 3, 4 and 5 and it explains the results for phases 2 and 5. Indeed, since a failure of the rod wad observed for phase 2 (133/1330N), it was expected to have a failure for phase 5 too (140/1400N), since the loads applied are greater. However, the rod did not fail after 2.5 million of cycles. With the constant life diagrams and the sines' criterion, it is clear that those two cases are limit cases: it is then difficult to predict the rod fatigue behaviour.

The Wöhler diagram of the MESA Rail™ rod can be sketched (figure 30) and compared to the experimental data (figure 31).

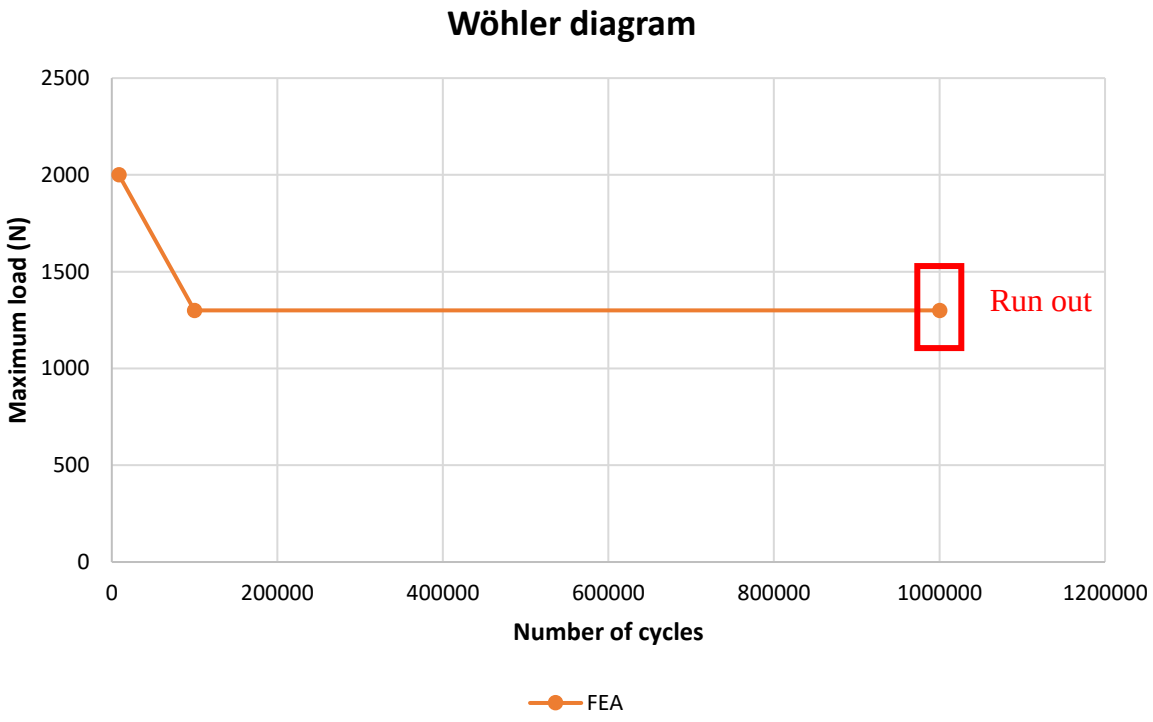

Figure 30: Wöhler diagram of the MESA Rail™ rod

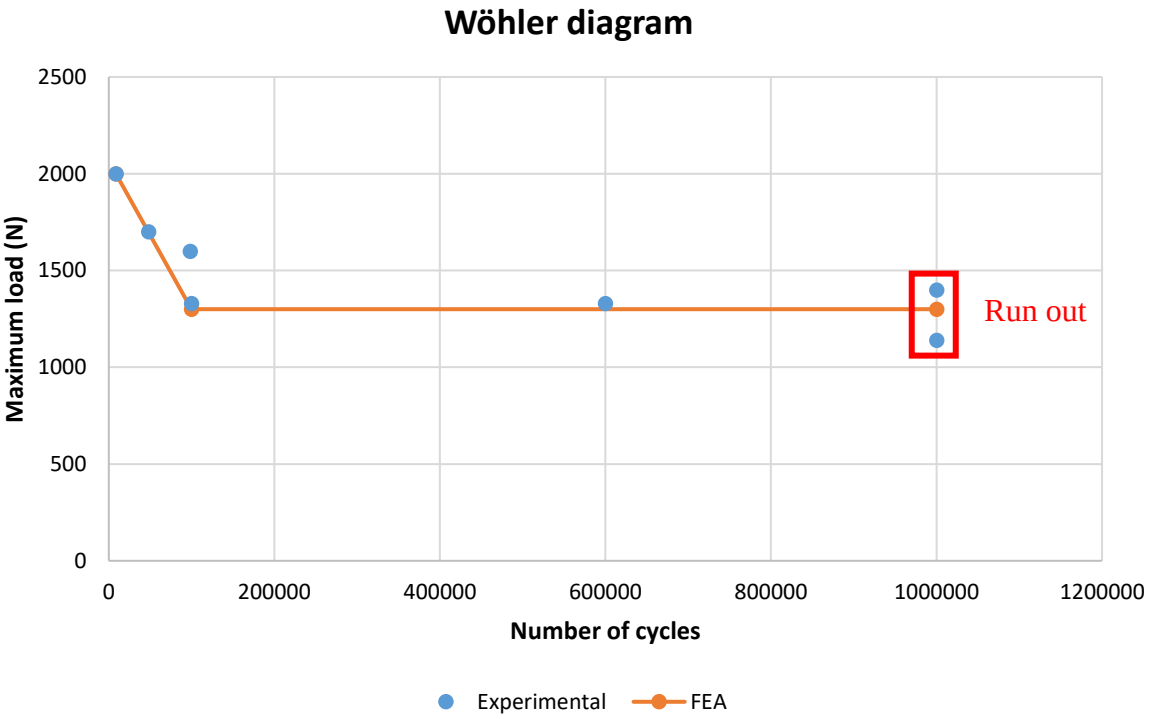

Figure 31: Wöhler diagram of the MESA Rail™ rod compared to the experimental data

Discussion and conclusion

The previous analysis allows to have a reliable model of the MESA Rail™ rod that leads to a relevant prediction of its fatigue behaviour, consistent with the experimental tests run during the previous work [3].

However, as previously said, studies have shown that the actual friction factor is 0.175. This difference could be explained by the fact that the material properties used are the one of a standard titanium alloy manufactured by K2M, but maybe not the material properties of the actual rod. Experimental tests should be performed to obtain them.

Moreover, the K parameter was assumed during these simulations. Using K=0.7, the conclusions are the ones done in the previous part. However, choosing a K=0.5, the rod fails for all the fatigue tests simulated. A first improvement should be to obtain the actual value of K with experimental tests (but the actual K seems to be closer to 0.7 since the results with this value are consistent with the experiments while the ones with 0.5 are significantly different). It is also possible to increase the MESA Rail™ rod fatigue strength thanks to methods like shot peening, generating residual stresses in the rod: since this kind of treatment is systematically applied, it should be added in the model to have better results (here, the margins of safety are overestimated).

It is also possible to perform an XRD analysis on the actual rod to get its internal state of residual stress.

Bibliography

- [1] “Residual Stresses in Titanium Spinal Rods: Effects of Two Contouring Methods and Material Plastic Properties”, Francesca Berti et al., 2018
- [2] “Computational and Experimental Fatigue Analysis of Contoured Spinal Rods”; Francesca Berti et al., 2019
- [3] “Caratterizazione meccanica di barre spinali in lega di titanio MESA Rail™”, Dario Crippa, Giada Porcelli and Caterina Villa, 2017
- Figure 1: https://cirqueacirca.com/human-spinal-cord-anatomy/human-spinal-cord-diagram-diagram-the-human-spinal-cord-human-spinal-cord-anatomy/
- Spine: https://en.wikipedia.org/wiki/Vertebral_column
- [4] Intervertebral discs: https://en.wikipedia.org/wiki/Intervertebral_disc
- Figure 2: https://www.pinterest.com/pin/515943701040714635/ Copyright© 2001 Benjamin Cummings
- [5] Degenerative disc disease: https://en.wikipedia.org/wiki/Degenerative_disc_disease
- [6] Spinal disc herniation: https://en.wikipedia.org/wiki/Spinal_disc_herniation
- [7] Vertebral osteochondrosis: https://en.wikipedia.org/wiki/Scheuermann%27s_disease
- [8] Osteoporosis: https://en.wikipedia.org/wiki/Osteoporosis
- [9] Scoliosis: https://en.wikipedia.org/wiki/Scoliosis

  “Breakthrough in three-dimensional scoliosis diagnosis: significance of horizontal plane view and vertebra vectors”, Tamás Illés, Miklós Tunyogi-Csapó, and Szabolcs Somoskeöy, 2011
- Figure 4: https://www.scoliosissos.com/news/post/s-curve-vs-c-curve-scoliosis-treatment

http://www.zimmerindia.com/medical-professionals/products/spine/st360-spinal-fixation-system.html

- [10] Nguyen et al. The fatigue life of contoured Cobalt-Chrome posterior spinal fusion rods. Proc. IMechE vol 225 part H: J. Engeneering Magazine (194- 198),14 May 2010
- K2M website: https://www.stryker.com/content/stryker/us/en/spine.html
- Figure 11: https://ryortho.com/breaking/new-in-spine-k2m-launches-rail-4d/ https://k2mmc.k2medical.com/mastercontrol/Main/MASTERControl/vault/view_pdf.cfm?ui=052619032501&infocardID=53BHGNB5KVGXTJEIVA
- [11] S. Masud et al. "Early Experience of the K2M Mesa Rail™ implant for spinal deformity correction." Orthopedic Proceedings, 20 October 2014.
- Fatigue: https://en.wikipedia.org/wiki/Fatigue_(material)
- Figure 10: https://community.plm.automation.siemens.com/t5/Testing-Knowledge-Base/The-Goodman-Haigh-Diagram-for-Infinite-Life/ta-p/410585
- [12] "Enhancing the Durability of Spinal Implant Fixture Applications Made of Ti–6Al–4V ELI by Means of Cavitation Peening,", Takakuwa, O., Nakai, M., Narita, K., Niinomi, M., Hasegawa, K., and Soyama, H., 2016
- [13] Shot peening: https://en.wikipedia.org/wiki/Shot_peening
- [14] "Rods in spinal surgery: a review of the literature", Hiroyuki Yoshihara, 2013
- [15] "Fatigue behavior of ultrafine-grained Ti–6Al–4V 'ELI' alloy for medical applications", L.R.Saitova, H.W.Höppel, M.Göken, I.P.Semenova, G.I.Raab, R.Z.Valiev
- [16] "Assessment of symptomatic rod fracture after posterior instrumented fusion for adult spinal deformity." Smith JS, Shaffrey CI, Ames CP, Demakakos J, Fu KM, Keshavarzi S, Li CM, Deviren V, Schwab FJ, Lafage V, Bess S; International Spine Study Group, 2012

- [17] “Notch sensitivity of titanium alloy, commercially pure titanium, and stainless steel spinal implants.”, Dick JC, Bourgeault CA., 2001
- [18] Kyphosis: https://en.wikipedia.org/wiki/Kyphosis